Flower-like-shaped manganese-doped $\alpha_v\beta_3$-integrin-ligand-functionalized SPIONs efficiently induce intracellular heat after AMF-exposition triggering cell death in a glioma cell line.

S. Del Sol-Fernández[1,#], Y. Portilla-Tundidor[2,#], L. Gutiérrez[3], O.F. Odio[1], E. Reguera[1,], D.F. Barber[2,*], M.P. Morales[4,*].*

[1]*Instituto Politécnico Nacional, Centro de Investigación en Ciencia Aplicada y Tecnología Avanzada, Unidad Legaria (CICATA-Legaria), Calz Legaria 694, Col. Irrigación, 11500 Ciudad de México, México.*

[2]*Department of Immunology and Oncology and Nanobiomedicine Initiative, Centro Nacional de Biotecnología, (CNB-CSIC), Darwin 3, 28049 Madrid, Spain.*

[3]*Departamento de Química Analítica, Universidad de Zaragoza, Instituto de Nanociencia de Aragón, Instituto de Ciencia de Materiales de Aragón (ICMA-CSIC) and CIBER-BBN, Mariano Esquillor, s/n, 50018 Zaragoza, Spain.*

[4]*Department of Energy, Environment and Health, Instituto de Ciencia de Materiales de Madrid (ICMM-CSIC), Sor Juana Ines de la Cruz 3, 28049 Madrid, Spain.*

AUTHOR INFORMATION
Co-senior authors and corresponding authors
*E-mail: puerto@icmm.csic.es (M.P.M)
*E-mail: dfbarber@cnb.csic.es (D.F.B)
*E-mail: edilso.reguera@gmail.com (E.R)

Author Contributions
[#]This author contributed equally to this work.

ORCID

S. Del Sol-Fernández (0000-0002-7660-966X)
Y. Portilla-Tundidor(0000-0003-2738-0384)
L. Gutiérrez (0000-0003-2366-3598)
O.F. Odio (0000-0002-0092-089X)
E. Reguera (0000-0002-4452-9091)
D.F. Barber (0000-0001-8824-5405)
M.P. Morales (0000-0002-7290-7029)

ABSTRACT

Despite the potential of magnetic nanoparticles to mediate intracellular hyperthermia when exposed to an alternating magnetic field, several studies indicate that the intracellular heating capacity of magnetic nanoparticles depends on factors such as the cytoplasm viscosity, nanoparticle aggregation within subcellular compartments, and dipolar interactions. In this work, we report the design and synthesis of monodispersed flower-like superparamagnetic manganese iron oxide NPs with maximized SAR and evaluate their efficacy as intracellular heaters in the human tumor-derived glioblastoma cell line U87MG. Three main strategies to tune the particle anisotropy of the core and the surface to reach the maximum heating efficiency were adopted: 1) Varying the crystalline anisotropy by inserting low amount of Mn^{2+} in the inverse spinel structure and 2) Varying NPs shape to add an additional anisotropy source, while keeping the superparamagnetic behavior, and 3) Maximizing NPs-cell affinity, through conjugation with a biological targeting molecule to reach the NPs concentration required to raise the temperature within cell. We investigate possible effects produced by these improved NPs under the AMF (f = 96 kHz, H = 47 kA/m) exposure in the glioblastoma cell line U87MG by monitoring the expression of *hsp70* gene and ROS production, as both effects have been described to be induced by increasing intracellular temperature. The induced cell responses include cellular membrane permeabilization and rupture with concomitant high ROS appearance and *hsp70* expression, followed by cell death. The responses were largely limited to cells that contained the nanoparticles and that were exposed to the AMF. Our results indicate that the developed strategies to optimize particle anisotropy in this work are a promise guidance to improve the heating efficiency of magnetic NPs in human glioma cell line.

KEYWORDS: manganese iron oxide nanoparticles, optimized uptake, intracellular hyperthermia, oxidative stress, cell death, biological responses to heat.

INTRODUCTION

Magnetic Hyperthermia Treatment (MHT), has emerged as a valuable treatment modality for certain types of cancers, in particular for those difficult to remove surgically such as brain tumors[1-2]. In this treatment, intracellular internalized nanoparticles (NPs) are exposed to an alternating magnetic field (AMF) that could trigger different effects such as intracellular heating, increasing the expression of the heat shock protein (HSP) family and induction of reactive oxygen species (ROS) through Fenton reactions. ROS can severely damage cellular structures like DNA, proteins, lipids, and cofactors of enzymes due to oxidation and, therefore, induce apoptosis[3-4]. Interestingly, concomitant with ROS production, an increase in fluidity and a loss of integrity of the cytoplasmic membrane that leads to the activation of cell death mechanisms that result in either necrosis or apoptosis has also been reported[5-6]. In addition, others effects such as the activation of dendritic and natural killer cells[7], and the increase of the lysosomal membrane permeability have also been associated with MHT[8]. Although the mechanisms, that lead to cell death are still not clear, the truth is that the complete regression of tumors in *in vivo* experiments with mice has been already achieved[9,10,11].

In MHT, magnetic nanoparticles (MNPs), considered as individual magnetic dipoles, orient their magnetic moments after exposure to an alternating magnetic field. The magnetic energy is dissipated through the relaxation of the nanoparticles moment to equilibrium, either through the rotation of the nanoparticle as a whole (Brownian relaxation) or through the rotation of the magnetic moment within the nanoparticle core (Néel relaxation)[12-13]. Remarkably, very high heating capacity has been obtained for flower-shape maghemite[14] or cube like shape NPs[15] or by varying the core-shell components of the nanoparticles

($CoFe_2O_4$@$MnFe_2O_4$, SAR=2280 W/g)[9]. However, it has been reported that NPs, once internalized in cells, show lower SAR values (ranging from 90 % down to 50% of the SAR measured in liquid), depending on the particle size, shape and composition[12,16]. This effect has been attributed to Brownian mobility restriction[16,17], or particle aggregation[18], including also the detrimental effect of viscosity on the obtained SAR[19]. In previous studies conducted in our laboratory it has been observed that the inefficiency of the NPs to respond to AMF is due to the compaction of NPs as large aggregates with random NPs orientation in the lysosomes of Pan 02 tumor cells[20]. In contrast, several groups have recently reported cell death after MHT treatment but with disagreements about perceptible changes or not in temperature during the treatment[21-23]. Besides the non-thermal damaging of tumour cells, there exist observations of thermal damaging effects. Zhang et al[6]. have found cell damaging effects using Herceptin-guided magnetic nanoparticles to malignant human mammary epithelial cells without observing significant temperature increase. According to Clerc et al[8], when using MHT with Gastrin-grafted NPs an increase of ROS is observed on the lysosomal surface which provokes lipid peroxidation, lysosomal membrane permeabilization and leakage of the lysosomal enzymes, including Cathepsin-B which activates caspase-1 but not apoptotic caspase-3. Also, other authors have described the generation of ROS on the cellular membrane, because of the exposure to AMF, which increases permeabilization and finally rupture, provoking death by necrosis in cells[24]. However, mechanical damage in the cell interior cannot be discarded if the nanoparticles are able to oscillate under the influence of the external alternating magnetic field[25]. Besides the promising prospective of hyperthermia, in clinical studies, the therapeutic outcome has resulted to be rather heterogeneous.

In order to shed some light on the effect of the MHT on cell viability, it is necessary to rationalize the design of NPs for MHT and to consider the different parameters governing their relaxation mechanism that can be divided between extrinsic (magnetic field amplitude and frequency) and intrinsic parameters (NPs size, structure and magnetic anisotropy)[1,26]. In concordance to this, two main strategies can be adopted to tune the effective particle anisotropy and therefore the heating efficiency: 1) Varying the crystalline anisotropy by inserting low number of Mn^{2+} cations in the inverse spinel structure and 2) Varying NPs shape to add an additional anisotropy source. Introducing Mn ions leads to the formation of manganese doped ferrite nanoparticles with high magnetization, which increases SAR values[27]. In addition, shape anisotropy can also be used to obtain higher SAR values, as it has been previously demonstrated for iron oxide nanocubes[12,15] and flower-like particles[14,28,29]. In fact, these last ones show some of the highest SAR values in the bibliography, over 3000 W/g due to collective magnetic behavior between the cores fused to form the particle[14]. Additionally, it is strongly desirable to reach the highest number of nanoparticles inside the cell, whereby a suitable coating and functionalization of the nanoparticles is necessary[29]. The cyclo(-RGDfK) cRGD peptide has been chosen because it is an effective ligand for targeting tumor microvasculature and cancer cells such as glioblastomas through the specific binding to the $\alpha_v\beta_3$ integrin, which is overexpressed on the cell surface in many tumors and tumoral cell lines[30,31,32,17]. It has been previously showed that cells expressing $\alpha_v\beta_3$ integrin, such as U87MG cells, are able to internalize higher amounts of iron oxide NPs functionalized with cRGD peptides when compared with cells that lack the expression of $\alpha_v\beta_3$ integrin such as L929 cells[33] or MCF-7 cell line[17,34] which is in concordance with the fact that the RGD peptide specifically interacts with $\alpha_v\beta_3$ integrin. This peptide has also been used combined with gold

NPs in U87MG showing fast endo and exocytosis processes of the NPs, dependent on the recycling of the with $\alpha_v\beta_3$ integrin, suggesting the importance of controlling the cell uptake profile with time[35].

In this work we investigate the effect of tuning particle anisotropy (magnetocrystalline and shape) to improve the heating efficiency of cRGD peptide functionalized monodisperse manganese-doped iron oxide NPs in a glioblastoma cell line. The NPs were designed for optimal SAR performance by optimizing the size and shape to obtain desirable high saturation magnetization, controlled collective magnetic interactions and, superparamagnteic behavior at room temperature, because this translates to higher heating rate per unit mass. Then, maximizing the cell-NPs affinity through biological targeting (cRGD peptide) we expect to have an adequate amount of cell-internalized SPIONs to induce intracellular heating in U87MG. We have analyzed biological effects of cRGD peptide functionalized manganese iron oxide NPs-loaded U87MG cells under an alternating magnetic field, assessing the expression of *hsp70* gene and ROS generation, the correlation between ROS production and membrane stress and rupture, as well as the possible activation of cell death pathways.

RESULTS AND DISCUSSION

Mn-doped iron oxide nanoparticles were initially synthesized by the thermal decomposition of iron and manganese acetylacetonate in 1-octadecene and in presence of oleic acid (OAc) and oleylamine (OAm). Then, the resultant hydrophobic nanoparticles (**NF-OA**) are transferred to aqueous medium by a ligand exchange reaction with DMSA ligand (**NF-DMSA**). Finally, cyclo(-RGDfK) peptide is conjugated to the system (**NF-DMSA-PEP**) in order to improve the cellular internalization of the nanoparticles. These functionalization steps are represented in Figure 1a. ICP-OES has been used to measure the metal content of the inorganic phases in order to determine the manganese doping level of the ferrites in accordance with the formula $Mn_xFe_{3-x}O_4$. Results yielded that hydrophobic and hydrophilic nanoparticles occur as $Mn_{1.1}Fe_{1.9}O_4$ and $Mn_{0.8}Fe_{2.2}O_4$, respectively. In the first case, the final Fe/Mn molar ratio is near to the initial molar ratio of the metal precursors. The decrease of the Mn doping level after the ligand exchange reaction has been reported previously[36]. On the contrary, after peptide conjugation the metal composition of the inorganic core does not present a significant variation, but a slight decrease in Mn content resulting in the formula $Mn_{0.7}Fe_{2.3}O_4$.

Figure 1b shows the FT-IR spectra of the three nanostructured systems. In the case of **NF-OA**, the dominant signals appear in the range of 2800-3000 cm^{-1} and at 1463 cm^{-1}, which correspond to the ν(C-H) and δ(CH_2) modes, respectively, of the abundant alkyl groups of OAc and OAm molecules at the surface of the ferrites. OAc is expected to be predominantly anchored to the surface cations, which is confirmed by the presence of a broad peak at 1560 cm^{-1} accounting for the ν_{as}(COO) mode of the metal carboxylates; also free OAc molecules

forming a second surfactant layer are observed due to the occurrence of the ν(C=O) mode at 1740 cm^{-1}. The band centered at 568 cm^{-1}, characteristic of lattice Fe-O vibrations in spinel ferrites, denotes the formation of the inorganic phase. After the surface modification from **NF-OA** to **NF-DMSA**, it is noted a dramatic reduction of the alkyl signals and the merging of two intense and broad bands centered at 1590 and 1400 cm^{-1}, which correspond to the ν_{as}(COO) and ν_{s}(COO) modes of metal carboxylates, respectively. Such signals arise due to either the anchoring of the DMSA carboxylic groups to the ferrite surface or the free carboxylates pointing toward the aqueous medium, and together indicate the successful ligand exchange reaction which makes possible the aqueous dispersion of the nanoparticles. It is worth to note the absence of the ν(S-H) mode, which suggests the formation of intermolecular disulfide bridges during the exchange reaction. The inorganic phase is retained, as can be noted from the band at 584 cm^{-1}; in this sense, the powder XRD (see Figure 1c) displays the characteristic pattern of the inverse spinel structure, as compared with the $MnFe_2O_4$ phase (COD 96-230-0619). Finally, cyclo(-RGDfK) peptide was incorporated into the nanoplatform by the conjugation of the lysine amino end group with the free carboxyl moieties of the **NF-DMSA** sample by using EDC/SulfoNHS as coupling protocol. The FT-IR spectrum of the resulting **NF-DMSA-PEP** sample shows new distinct features superimposed to the signals from the **NF-DMSA** sample that belong to the peptide (see Figure S1): the broad band centered at 1640 cm^{-1} with a shoulder around 1580 cm^{-1} correspond to the ν(C=O) and δ(N-H) modes, respectively, of the amide functions; moreover, the intense signals near 1200 and 1100 cm^{-1} account for ν(C-N) vibrations due to the abundant C-N bonds.

Further hints about peptide conjugation to the nanomaterial can be drawn from hydrodynamic size and zeta-potential measurements. The average hydrodynamic size grows

from 57 to 184 nm (see Figure 1d), while the zeta-potential (measured under physiological conditions) becomes less negative (from -46 to -34 mV). Such marked differences between **NF-DMSA** and **NF-DMSA-PEP** samples suggest that peptide inclusion was successful. Moreover, from the combination of both results it is apparent that peptide assembly not only contributes to an increase in the nanosystem size, but also decreases the nanoparticle surface charge, which in turn could favor the formation of some aggregates; however, the value of -34 mV still provides good colloidal stability. The peptide conjugation efficiency was 49% under our experiment conditions, as calculated using the Equation 1 in Experimental Section**.** We estimated that the amount of conjugated cyclo(-RGDfK) peptide was 37 molecules for each NP (see section S2 in SI).

Since **NF-DMSA** and **NF-DMSA-PEP** samples are proved for *in vitro* hyperthermia treatment, we first register the field-dependent magnetization curves (M-H) at room temperature (290 K), as shown in Figure 1e. Given the similar superparamagnetic behavior of both samples, it is apparent that peptide conjugation does not affect the magnetic properties of the nanoflowers. The high Ms values (around 98 $Am^2/kg_{(Fe+Mn)}$), which are higher than those reported for other nano-magnetic platforms based on $MnFe_2O_4$ nanoparticles, are expected to favour a high heating efficiency under an AMF[14, 28]. Besides, both exhibit values of coercitivity and remanence close to zero (see Table 1 in SI), thus confirming the onset of the superparamagnetic regime at this temperature. In contrast, the samples display a clear ferrimagnetic behavior at 5 K (see Figure S3 in SI).

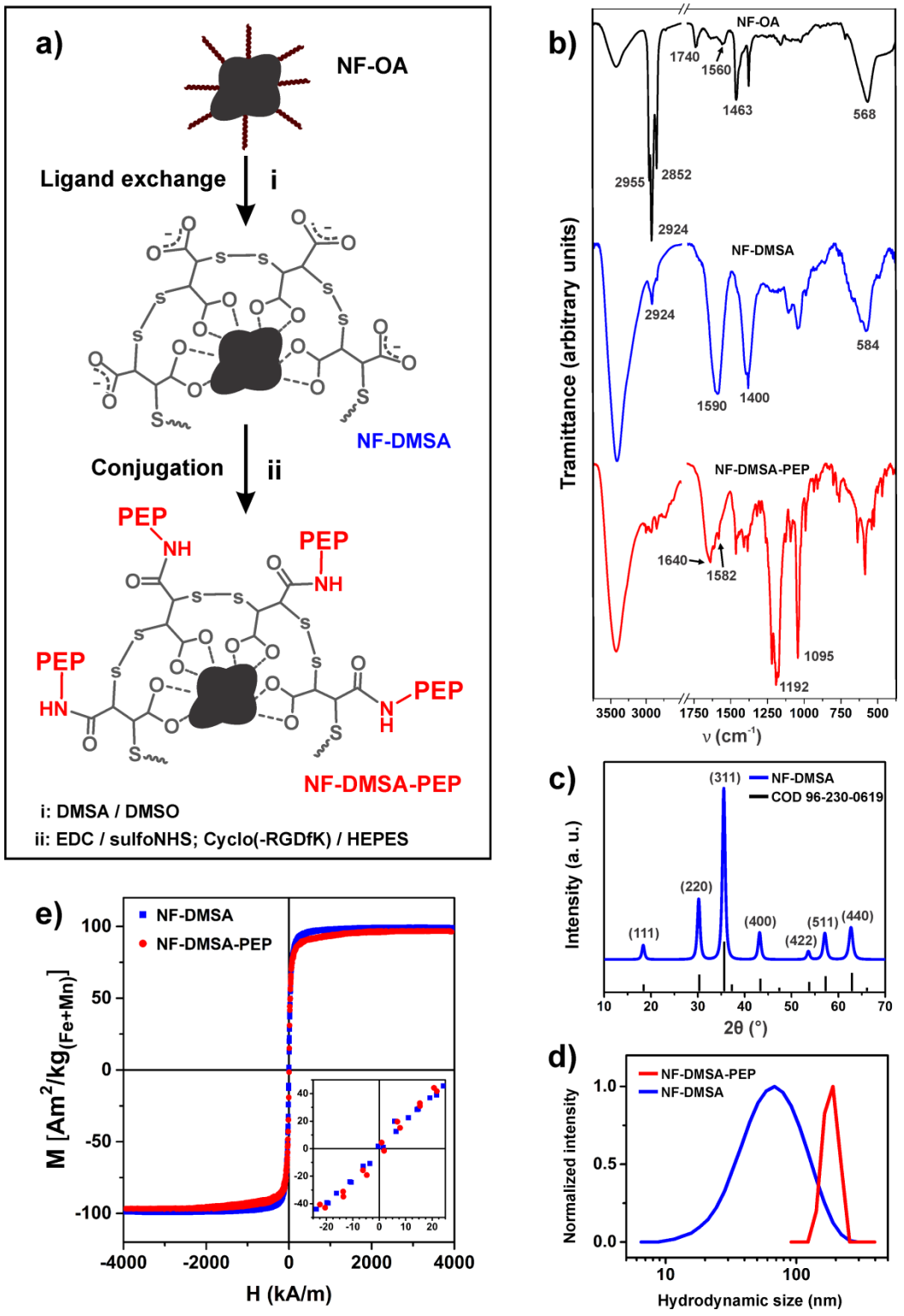

Figure 1. Design and characterization of the synthesized nanosystems (**a**) Scheme of DMSA functionalization and peptide conjugation of the NF. (**b**) FTIR spectra of NF-OA, NF-DMSA and NF-DMSA-PEP samples. (**c**) Powder XRD of NF-DMSA sample (the reference diffractogram corresponds to the $MnFe_2O_4$ phase [COD 96-230-0619]) and (**d**) Hydrodynamic size distribution for NF-DMSA and NF-DMSA-PEP

samples. (**e**) Hysteresis loops recorded at 290 K for NF-DMSA and NF-DMSA-PEP samples. Inset: low field hysteresis loops.

Figure 2 focuses on the size and morphology of the synthesized nanosystems. TEM images (Figure 2a) reveal that the initial **NF-OA** sample consists of irregular flower-like particles with an average diameter of (18.3±1.9 nm); the size distribution is narrow and follows a log normal behavior. HRTEM image in the left panel of Figure 2b evidences that the nanoparticles present good crystallinity and do not entail single cores, but they are likely formed by the fusion of a small number of grains. This finding is supported by the fact that the crystallite size determined with the Scherrer formula from the XRD pattern is 9 nm, which is almost half of the average nanoparticle diameter. However, the resulting Fourier Transformation of the HRTEM image (right panel of Figure 2b) gives a pattern typical for single crystals in which it is possible to identify several planes like the (111), (220) and two of the {311} family. Such diffraction coherence suggests that the grains forming the nanoflowers are coupled by strong superexchange magnetic interactions; these interactions arise due to the experimental conditions employed for the synthesis of the ferrite nanoparticles, which influence the growth of the crystals. Thus, a relatively small molar ratio between the metal precursors and the surfactants, combined with an equimolar mixture of OAc and OAm, could promote a preferential growth of the initial seeds along certain crystal directions normal to the facets poorly stabilized by the surfactants (mainly those stabilized by OAm molecules). Such grains bearing highly magnetic "active" facets are then prone to couple in a ferromagnetic fashion with other similar grains, giving rise to the observed irregular flower-like shape of the final nanoparticles.

Figures 2c and 2d shows the STEM and HRTEM images of the **NF-DMSA** sample; the size distribution, morphology and crystallinity of the nanoparticles are barely unaltered after the

ligand exchange reaction; however, it provokes an apparent decrease in the interparticle distance due to a smaller effective steric hindrance after substitution of OAc by DMSA molecules. The relation between the average particle diameter calculated by microscopy (17.0 ±1.6 nm) and the average crystallite size computed by XRD (12 nm) supports the same internal particle structure outlined for the **NF-OA** sample. It is interesting to note that in both systems the individual nanoparticles are not spatially random distributed, but they tend to exhibit a certain self-organization level that produces an anisotropic spatial distribution, which can be explained due to the occurrence of strong interparticle dipolar interactions; indeed, ZFC/FC curves (see Figure S4) fully support this idea[26,37].

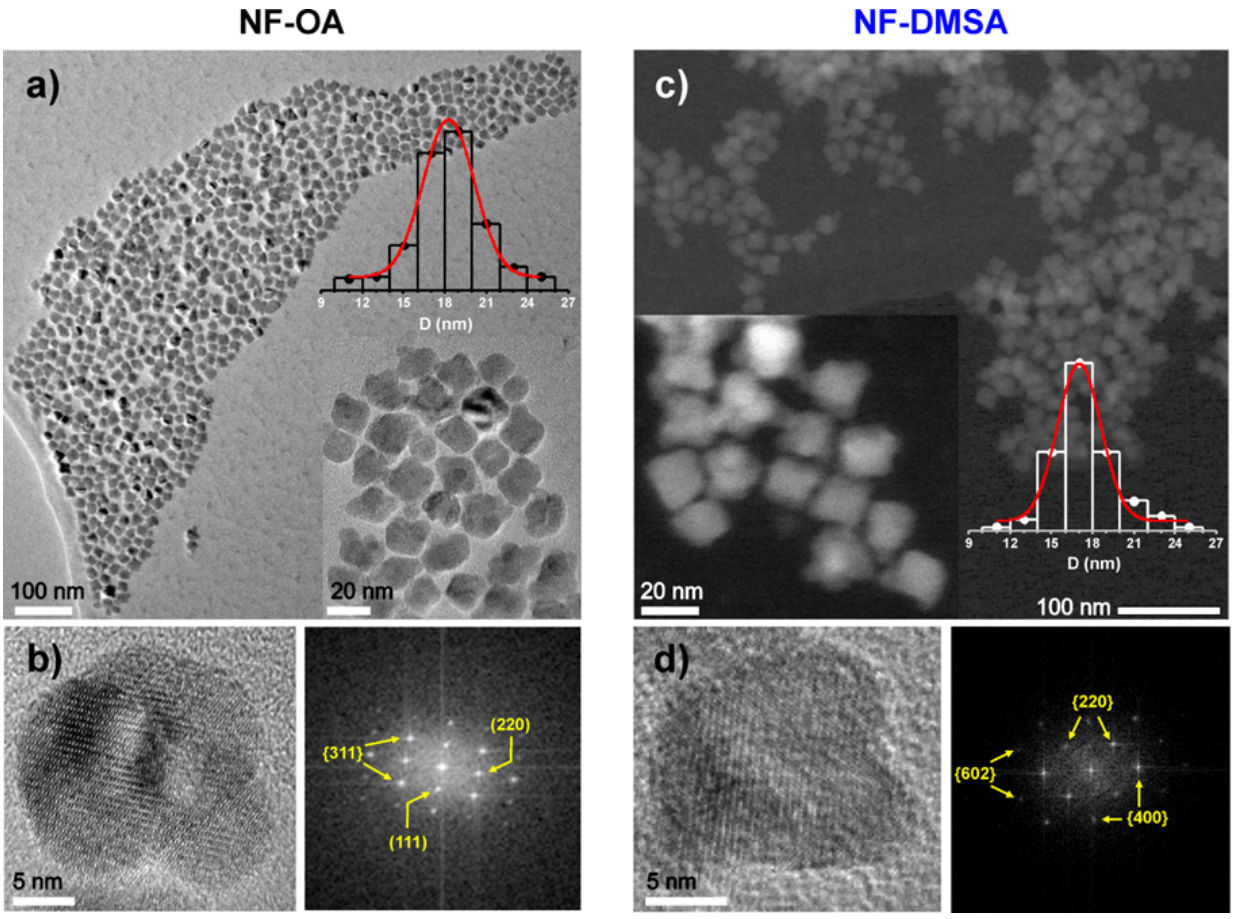

Figure 2. Microscopy study of NF-OA and NF_DMSA samples. (**a**) TEM micrographs (low and high magnification) and size distribution of NF-OA sample**.** (**b**) HRTEM (left) and Fourier Transformation showing the crystal planes (right) of a NF-OA particle. (**c**) STEM micrographs (low and high magnification) and size

distribution of NF-DMSA sample**.** (**d**) HRTEM (left) and Fourier Transformation showing the crystal planes (right) of a NF-DMSA particle.

By comparing the interplanar distances of the (220) plane for both nanosystems, it is apparent that the lattice spacing decreases from 0.295 to 0.285 nm after ligand exchange. This small but noticeable variation could be related to the decrease in the manganese doping level of the ferrite structure that was discussed above; this behavior agrees with other reported data[27].

In order to evaluate and compare the hyperthermia performance of the aqueous suspension of the obtained **NF-DMSA** nanosystem, two additional platforms were selected as references. Reference samples consist of 12 nm spherical magnetite nanoparticles coated with DMSA (**NP-REF**) obtained by coprecipitation[38,39] and 20 nm flower-like maghemite nanoparticles coated with citric acid obtained by the polyol method[40](**NF-REF**) (Figure S5 in SI). The change in temperature as a function of time was recorded using the equipment described in the experimental section, maintaining the nanoparticle concentration at 1 mg NP/mL and the applied field with $f = 96$ kHz and $H_0 = 47$ kA/m; with this values, the product $H_0 f$ lies below the biological discomfort level[41]. Figure 3a shows the resulting heating curves. First, it is worth to note the atypical heating curve of NF-DMSA ferrofluid at longer times with a non-monotonic increase, probably due to the formation of ordered chain-like structures[42-44], as it was observed in Figure 2c. More important, the three platforms produce a similar net increase in temperature, 11.4, 12 and 10.2 °C for NF-DMSA, NF-REF, and NP-REF, respectively; however, the initial slope is distinctly higher for the **NF-DMSA** sample. Consequently, this sample displays a superior heating capacity compared to the reference samples, which is reflected in the differences between the respective SAR values (689 *vs* 424

and 94 $W/g_{(Fe+Mn)}$), as it is shown in Figure 3b (calculated using the Equation 2 in Experimental Section). This great heating performance of **NF-DMSA** sample results from the combined increase in the magnetocrystalline and shape anisotropies of the nanomaterial due to the Mn-doping in the ferrite structure and the flower-like morphology, respectively. Besides, when the SAR value is converted to intrinsic loss power (ILP) in order to stablish proper comparisons[45], it shows up that the **NF-DMSA** value (3.2 nH) is superior to the values reported for 15 nm $MnFe_2O_4$ nanoparticles (0.6 nH) and comparable to core-shell $CoFe_2O_4$@$MnFe_2O_4$ nanostructure (3.3 nH), which has been successfully applied in the complete regression of glioma cell tumor in mice[9]. Moreover, SAR is only slightly reduced when particles are in a more viscous media such as 50 % water/glycerol mixture (Figure S6 in SI).

Wrapping up, the prepared NF-DMSA sample displays a high SAR value and superparamagnetic properties at room temperature, therefore being a promising candidate for hyperthermia therapy. However, apart of the heating efficiency of the NPs, there is another important requisite to make the magnetic hyperthermia treatment effective to induce the death of cancer cells, that is an elevated uptake of NPs by the cells that we expect to reach with the peptide-carrying sample (NF-DMSA-PEP), as it has been previously observed for others group[32-33,35].

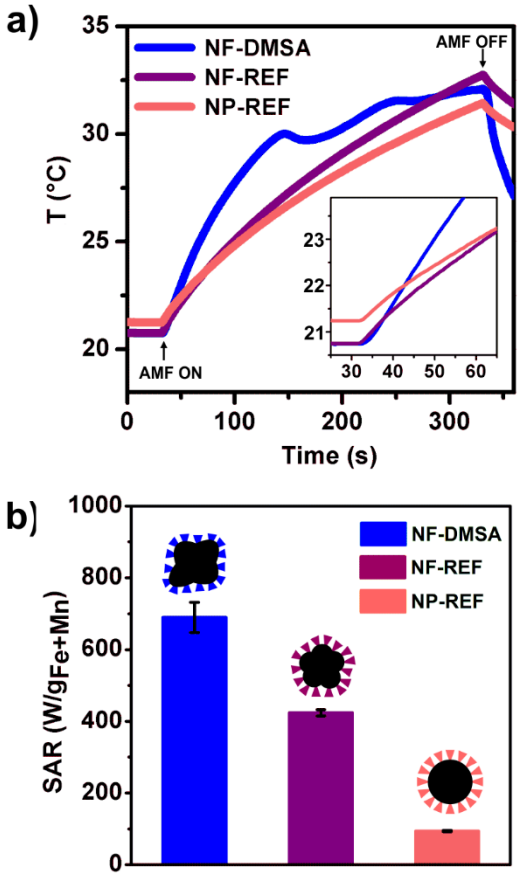

Figure 3. **Heating efficiency of aqueous suspensions** (**a**) Heating curves of aqueous solution of NF-DMSA and reference samples (NP-REF and NF-REF), all of them at concentration of (1 mg_{NP}/ml) under the same experimental condition (f = 96 kHz, H = 47 kA/m). The content of the magnetic ions for each sample were ([Fe] = 2.70 mg/m L for NP-REF), ([Fe] = 0.72 mg/mL for NF-REF) and ([Fe + Mn] = 0.76 mg/mL). Inset: Zoom of the initial linear slope. (**b**) SAR values of colloidal samples (with standard deviation).

Mn-doped NF are safe. To examine nanoparticle toxicity, different assays have been used to evaluate cell survival after incubation with increasing concentrations of NF-DMSA or NF-DMSA-PEP from 0 to 100 μg/mL in $\alpha_v\beta_3$ integrin-overexpressing U87MG cells (Figure 4). PrestoBlue analysis has shown that U87MG cells viability is higher than 90% after incubation with NF-DMSA or NF-DMSA-PEP at any tested iron concentration (Figure. 4a). Since Presto Blue indirectly measures mitochondrial metabolism, these results suggest that nanoparticles do not induce any relevant alteration in the cellular metabolism.

Alternatively, apoptosis induction in U87MG cells after incubation with increasing concentrations of NF-DMSA or NF-DMSA-PEP have also been evaluated by TUNEL assay (Figure 4b, c).

Quantification of TUNEL positive cells showed no statistically significant differences for any tested concentrations (Figure 4c). Annexin V-FITC/PI staining to differentiate between cell death induced by apoptotic or necrotic processes has also been performed (Figure S7). Even at the highest iron concentrations (100 μg/ml) no significant differences among the amount of viable, apoptotic and necrotic cells between the two groups of cells and the controls have been observed.

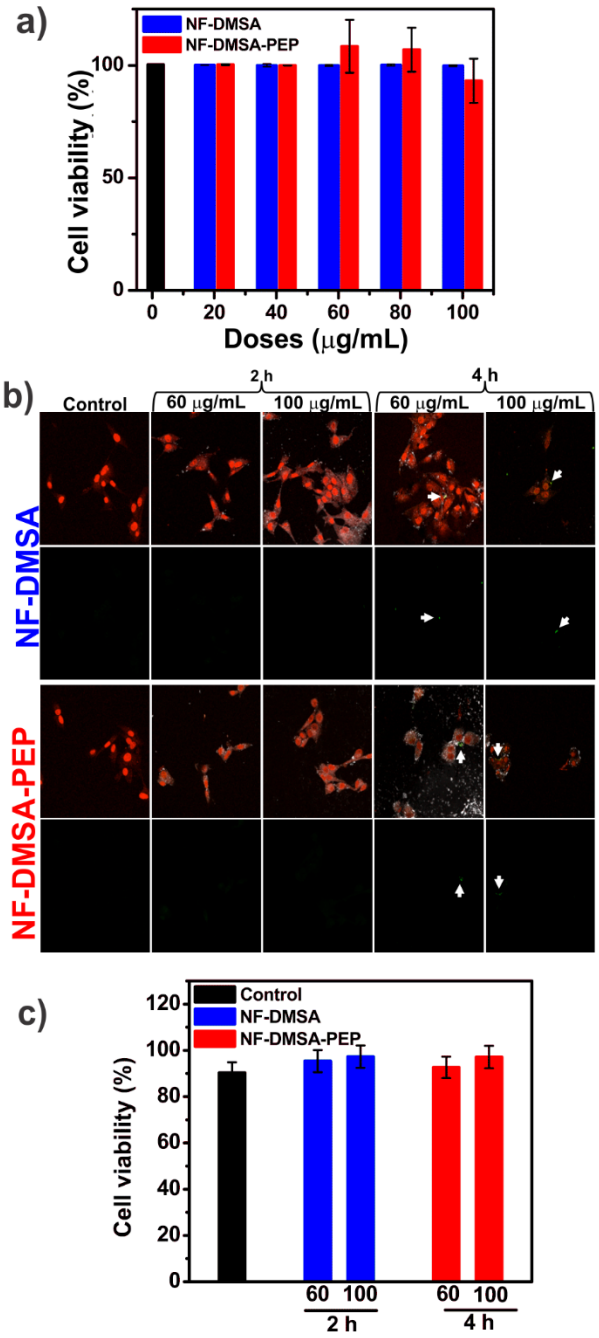

Figure 4. **NPs toxicity in U87MG cells.** Cell viability percentages of U87MG cells after incubation with different NPs concentrations as determined by PrestoBlue assay (**a**) or by TUNEL staining (**b, c**). Quantification of apoptotic cells (green staining) and live cells (red-staining) in TUNEL images (b) was used to calculate cell viability shown in panel (c). Data were normalized to untreated cells and are shown as mean ± SD (3 independent experiments by triplicate) in both analyses. Two-way ANOVA showed no statistically significant differences.

All these results have shown that the incubation of U87MG cells with NF-DMSA or NF-DMSA-PEP does not affect their viability at any of the tested concentrations as determined by different assays. In addition, the functionalization of the nanoparticles with the peptide cRGD does not increase cell death neither.

cRGD peptide increases the nanoparticles uptake in U87MG human glioblastoma cancer cells, and the internalization follows cycles of endocytosis and exocytosis. As previously mentioned, two of the main requirements for magnetic hyperthermia induction of death in cancer cells are the use of NPs with high heating efficiency and the need to reach a high number of internalized NPs inside the cell[29]. For this reason, to reach the NPs concentration required to raise the temperature within the cell, the cRGD peptide has been chosen as targeting ligand.

To test whether the functionalization of NF-DMSA with the cRGD peptide improved the nanoparticles internalization, first U87MG cells have been incubated with NF-DMSA or NF-DMSA-PEP for different periods of time (0, 2, 4, 8 and 24 h) with different concentrations of each NPs type. The amount of particles uptaken has been followed by the determination of the iron content measured by ICP-OES (Figure S8).

Both systems, with and without the peptide exhibit very different loading kinetics. In U87MG cells incubated with 60 μg/mL of NF-DMSA, the maximum Fe uptake have been observed at 2h (41.67 pg Fe/cell) and 4h (42.36 pg Fe/cell); but decrease at 8 h (30.66 pg Fe/mL) and more accentuated at 24 h (16.88 pg Fe/mL). For NF-DMSA-PEP, a maximum Fe uptake has been observed at 2 h (260 pg Fe/cell), being reduced at 4 h (143.64 pg Fe/cell), re-increased at 8 h (176.13 pg Fe/cell) and re-decreased again at 24 h (49.82 pg Fe/cell). This profile resembles what has already been described for cRGD-functionalized gold NPs in

U87MG cells[35], where continuous cycles of endocytosis/exocytosis occur due to $\alpha_v\beta_3$ integrin recycling, increasing and decreasing alternatively NPs uptake along incubation time. Based on the results from this kinetic study we have selected the first cycle of the loading kinetics (2 and 4 h) for further analysis because it was the one exhibiting the highest Fe cellular uptake. Then, we have analyzed the NPs internalization, with and without the peptide, at three different concentrations (40, 60 and 100 μg/ml) (see Figure 5a). This analysis showed that cells incubated with the highest concentration (100 μg/ml) of cRGD-modified nanoparticles (NF-DMSA-PEP) internalized more particles, reaching the highest iron content, that is 764.6 pg Fe/cell and 271.33 pg Fe/cell at 2 and 4 h, respectively. The efficacy of cRGD peptide functionalization in NPs uptake is clear when comparing its uptake with that for non-functionalized NPs, where a 6-fold difference in NPs internalization at 2 h for 60 μg/ml has been observed. The ratio of internalization is reduced to half at 4 h for the same concentration. Similar high uptake values (a 4-fold increase) were observed in U87MG treated with cRGD-fused magnetosomes when compared with non-modified magnetosomes[17]. These results together with the kinetics profile described above strongly suggest cycles of endocytosis/exocytosis of the cRGD-modified NPs.

To study NPs cellular localization in U87MG cells we have used different approaches. First, confocal microscopy, has shown that regardless their coupling with the peptide, particles were mainly accumulated in the cytoplasm at 2 and 4 h (Figure 5b). In addition, at 4 h more NPs were also detected outside the cells in the culture media compared to the same observations at 2 h, which is in concordance with the peptide-mediated NP recycling process mentioned along this section.

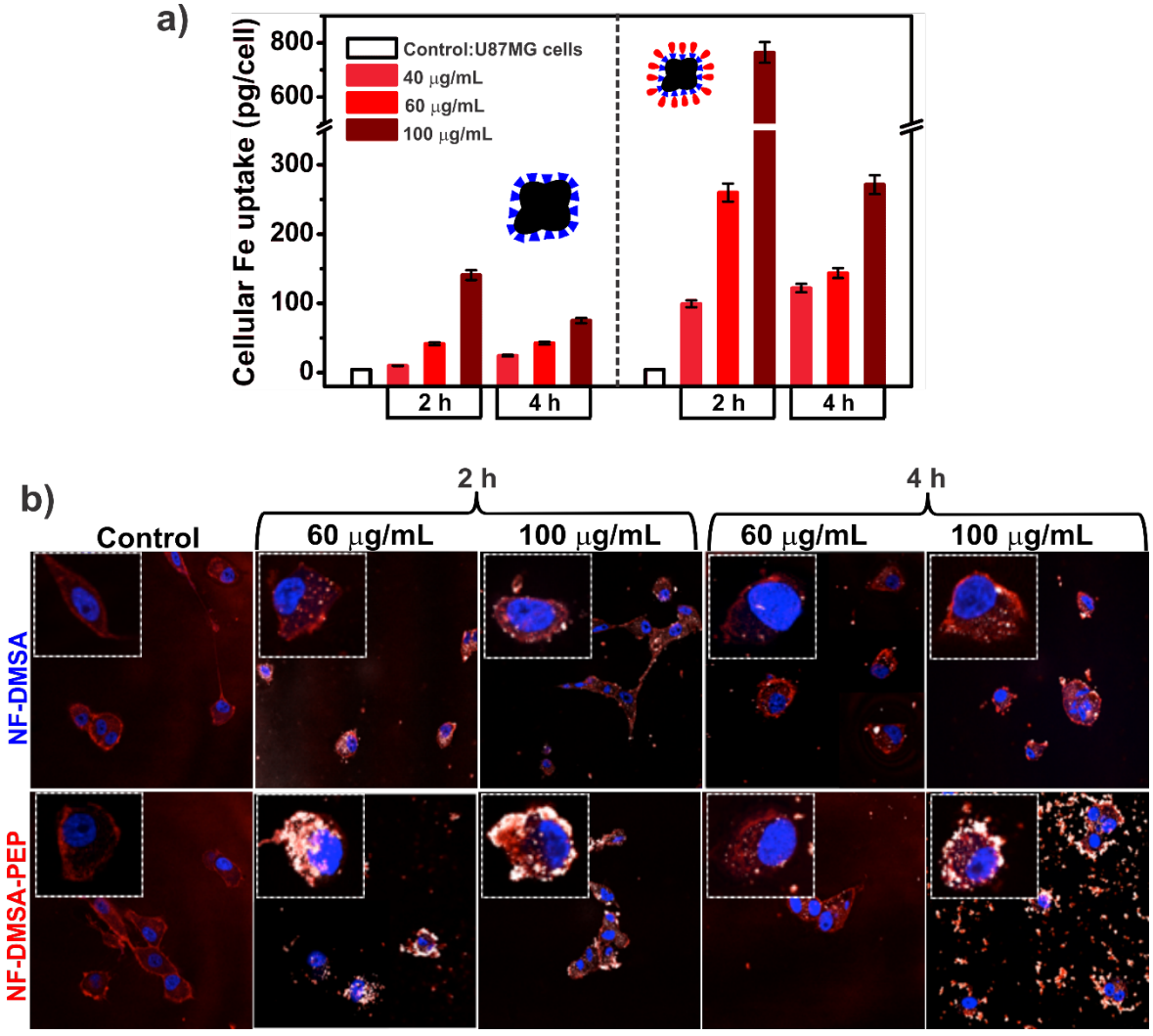

Figure 5. **Iron cellular uptake and subcellular distribution of NPs on U87MG cells.** (**a**) Quantification of iron concentration by ICP-OES. The total amount of iron was divided by the number of cultured cells for each sample. Data are shown as mean ± SD (n = 3). (**b**) Images of U87MG cells loaded NPs (60 and 100 μg/ml) acquired by confocal microscopy (cell membrane (red), nuclei (blue) and NPs (gray)) (scale bar =10 μm).

Next, subcellular localization of the particles in U87MG cells after incubation with NF-DMSA and NF-DMSA-PEP for 0, 2 and 4 h was analyzed by TEM (Figure 6). TEM images showed the presence of intracytoplasmic NPs aggregates when U87MG cells were incubated for 2 h with NF-DMSA (Figure 6b). TEM images obtained after 4 h incubation showed almost similar number of intracytoplasmic aggregates (Figure 6c). TEM images of the U87MG cells after incubation with NF-DMSA-PEP showed more NPs aggregates at 2 h than

cells incubated with NF-DMSA, which agrees with our previous data, and with the cRGD peptide functionalization (Figure 6e). TEM images obtained after 4 h incubation showed almost no intracellular aggregates but many smaller NPs aggregates near the cell membrane or outside the cell suggesting that the NPs uptaked at 2 h were exocytosed at 4 h (Figure 6f)[35].

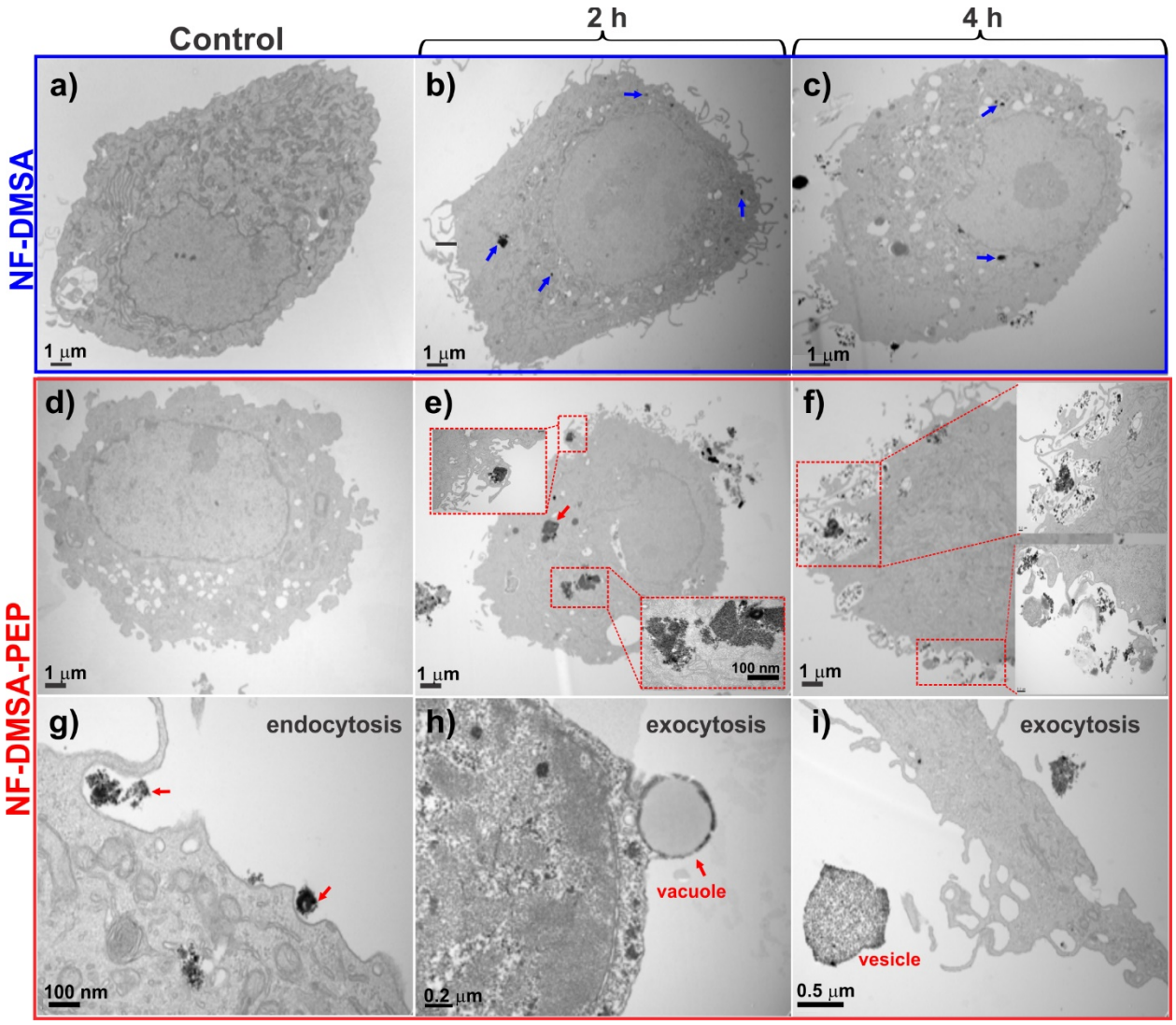

Figure 6. NP subcellular localization in U87MG cells. Representative TEM image of U87MG cells before NPs incubation (**a**, **d**). TEM images of U87MG cells incubated with NF-DMSA for 2 h or 4 h (**b**, **c**), and with NF-DMSA-PEP for 2 h or 4 h (**e**, **f**). Magnification of features to illustrate the endocytosis and exocytosis dynamics observed in cells loaded-NF-DMSA-PEP (**g, h, i**).

In previous studies NPs are frequently found in compact aggregates inside lysosomes as consequence of their endocytic process, where they stay till they are degraded by the

lysosomal machinery[20]. In the case of U87MG cells TEM images showed that NPs aggregates were observed in multivesicular bodies, early endosomes or macropinosomes and then, most of them were exocytosed by the cells.

A schematic representation of the mechanism is illustrated in Figure 7. Generally, tumor cells and macrophages internalized nanoparticles by different routes of endocytosis: macropinocytosis, clathrin-dependent endocytosis, among others[46-49]. Then the magnetic nanoparticles are accumulated in endosomes and lysosomes, and finally they are degraded by the cells (Pathway 1). However, there is another cellular path for NPs targeting $\alpha_v\beta_3$ integrins receptor that involves recycling of integrins and consequent exocytosis process[50]. Here, for glioblastoma cells, the NPs could be endocytosed by a predominant macropinocytosis route (Figure 6e, g). The surrounding fluid and particles can be internalized into the macropinosomes. In macrophages, after separating from the membrane, macropinosomes move into the cytosol and fuse with lysosomes[46]. In contrast, in human U87MG cells, the macropinosomes travel back to the cell surface of the membrane and release the contents inside of vacuoles or vesicles with sizes in the range between 800 nm and 2 μm to the extracellular space (Figure 6h and i, and Pathway 2 in Figure 7). Internalization pathways are important to consider in order to choose a favorable protocol for the application of NPs in biomedicine, specifically in hyperthermia treatment because the cell NPs uptake is one of the key factors for the therapy success.

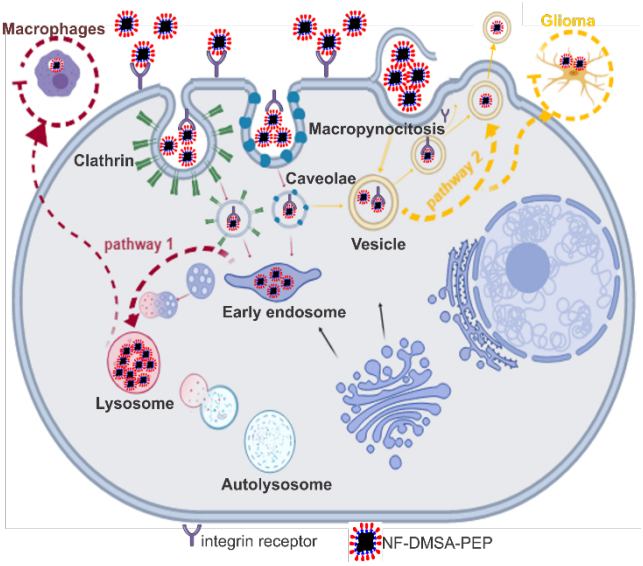

Figure 7. Scheme comparing the NPs intracellular trafficking network in for two pathways depending from cellular type.

The exposition of NPs-loaded U87MG cells to an AMF causes several biological effects.

It has been described that when cells with internalized NPs are exposed to an AMF, the NPs can generate heat, which dissipates to the cytoplasm resulting in an induction of the transcription of heat shock proteins 70 (*hsp70*)[51,52]. Moreover, it has also been reported that under exposition to an AMF cell-internalized NPs can directly induce ROS generation through Fenton reactions on the NP surface[8,53]. In this regard, ferrite NPs have been exploited as an efficient catalyst for decomposition of H_2O_2[54]. Increased levels of ferrous ions might form and react with H_2O_2 which causes various kinds of oxidative damage to DNA[3]. Alternatively, intracellular ROS induction may be attributed to NPs-cell interactions. In our system we have observed that NPs (NF-DMSA-PEP) are in close interaction with the cell membrane, probably due to their functionalization with the cRGD peptide, so the most probable effects could be the membrane permeabilization and the cellular integrity loss, triggering cell death by necrosis or/and apoptosis processes. To evaluate whether the

exposition of the U87MG-internalized NPs to an AMF induces any of the mentioned effects, we have carried out specific analysis to measure the degree of induction of each of them.

As already mentioned, thermal stress induced the transcription of *hsp70*, what allows us to use the analysis of *hsp70* transcriptional activation as molecular thermometer in cells[51]. First, we have tested if U87MG cells transcribed *hsp70* in response to a general thermal stress. For this analysis, cells have been incubated in a water bath at 42 ºC for 30 minutes, then cells have been kept 30 minutes in an incubator at 37 ºC under culture conditions, and finally total RNA has been extracted to generate cDNA that has been used as template for quantitative PCR analysis using specific primers (Figure 8a). This experiment has shown clear induction of mRNA *hsp70* transcription demonstrating the sensitivity of *hsp70* to heat in U87MG cells.

Because in previous studies we have seen that spherical iron oxide NPs coated with DMSA (NP-REF) were unable to induce *hsp70* transcription when internalized in Pan02 cells and exposed to an AMF (25 kA/m, 250 kHz)[20], we have included this NP-REF in the analysis for comparison. We have also included magnetite flower-like NPs coated with citrate (NF-REF) to compare with our flower-like manganese iron oxide cRGD-functionalized NPs (NF-DMSA-PEP). For the *hsp70* mRNA transcription analysis in all the experimental conditions, U87MG cells have been first incubated for 2 and 4 h with 60 μg/mL of either NP-REF, NF-REF, NF-DMSA, or NF-DMSA-PEP. After this incubation period, cells have been washed 3-times to remove not internalized NPs from the culture medium. Then, NPs-loaded cells have been exposed to the AMF (47 kA/m, 96 kHz) for 1 h. After AMF exposition, cells have been kept 1 h in standard culture conditions to allow *hsp70* transcription. In addition, to evaluate any possible effect on *hsp70* mRNA transcription due to the exposition of U87MG cells to the AMF, these cells (without internalized NPs) have been used as controls, exposed

to the AMF and processed under the same experimental conditions (Figure 8a). In U87MG cells exposed to the AMF without internalized NPs no *hsp70* mRNA transcription has been observed. Similarly, in U87MG cells incubated for 24 hours with either NP-REF, NF-REF, NF-DMSA or NF-DMSA-PEP, but not exposed to the AMF, no *hsp70* mRNA transcription has been observed neither.

The analysis of the expression level of *hsp70* in U87MG cells incubated for 2 h with the different NPs exposed to the AMF for 1 h, and left in the incubator for 1 h at 37ºC, has shown that NP-REF (spherical-like shape) do not induce mRNA *hsp70* transcription ($2^{-\Delta\Delta C_t}$ value of 0.78), that NF-REF (flower-like shape) induce a moderate expression of *hsp70* mRNA ($2^{-\Delta\Delta C_t}$ value of 12.63), that NF-DMSA (flower-like shape without the cRGD peptide) induce some *hsp70* mRNA expression ($2^{-\Delta\Delta C_t}$ value of 2.5), and that NF-DMSA-PEP (flower-like shape with the cRGD peptide) induce a strong *hsp70* mRNA expression ($2^{-\Delta\Delta C_t}$ value of 41.19), which is similar to the induction observed to the U87MG cells when they have been incubated in a water bath at 42 ºC for 30 minutes ($2^{-\Delta\Delta C_t}$ value of 51.11). In conclusion, when NF-DMSA-PEP have been exposed to the AMF, a similar *hsp70* transcriptional response to the one observed when external heat is applied to the cells has been observed, suggesting that this type of NPs could induce intracellular temperature increase.

Alternatively, the analysis of the expression level of *hsp70* in U87MG cells incubated for 4 h exposed to the AMF have shown again a larger expression of *hsp70* mRNA for NF-DMSA-PEP (flower-like shape with the cRGD peptide) in comparison to the rest of the samples ($2^{-\Delta\Delta C_t}$ value of 17.64) but reduced in comparison to the data observed at 2 h of incubation with the NPs (Figure 8a). The differences observed in the *hsp70* expression levels between 2 and 4 h of incubation with NF-DMSA-PEP or NP-REF reflect the differences

observed in NPs uptake due to the endocytosis/exocytosis dynamics that each NPs type follows (Figure 5 and Figure 6). According to this, the analysis of the iron content of the supernatant after incubation of NPs with cells for 2 and 4 h and after the exposition to AMF for 1 h quantified by ICP-OES indicated a minor amount of iron at 2 h (2.14 pg Fe/mL) than at 4 h (5 pg Fe/mL) supporting the idea that the internalized NPs have been exocytosed to the culture media mainly at 4 h, as reported for cRGD-modified gold NPs[35] (see, Figure S9.).

It is clear that only flower-like particles (NF-REF, NF-DMSA or NF-DMSA-P) induce *hsp70* expression in U87MG cells after exposition to a AMF, while for NP-REF, spherical-like shape with a size of 12 nm, no expression has been detected[16]. Although these results suggest that NPs shape could dictate the magnetic response to the AMF, it is also important to consider that size, size distribution and intracellular aggregation may have an important effect on the heating properties. In fact, the heating capacity of the particles measured in water (Figure 3b) does not correspond with the observations in cell cultures. These results are another indication of the difficulties of correlating the heating properties of particles measured in a test tube with their heating performance intracellularly. Heating efficiency is clearly associated in this work with the excellent characteristics of the NPs, whose anisotropy has been tuned for the field conditions, that is the large NPs size (18 nm), the Mn doping and its flower-like shape that provide a high SAR. In addition, the peptide coating prevents from further aggregation of the particles inside the cell. Aggregation of the NPs in lysosomes has been found to be responsible for the reduction of the heating efficiency of NPs after being cell-internalized, independently on the NPs size and shape or their initial SAR in aqueous media, as it was showed for magnetite cubes and spheres with high and low SAR values in water[15,20]

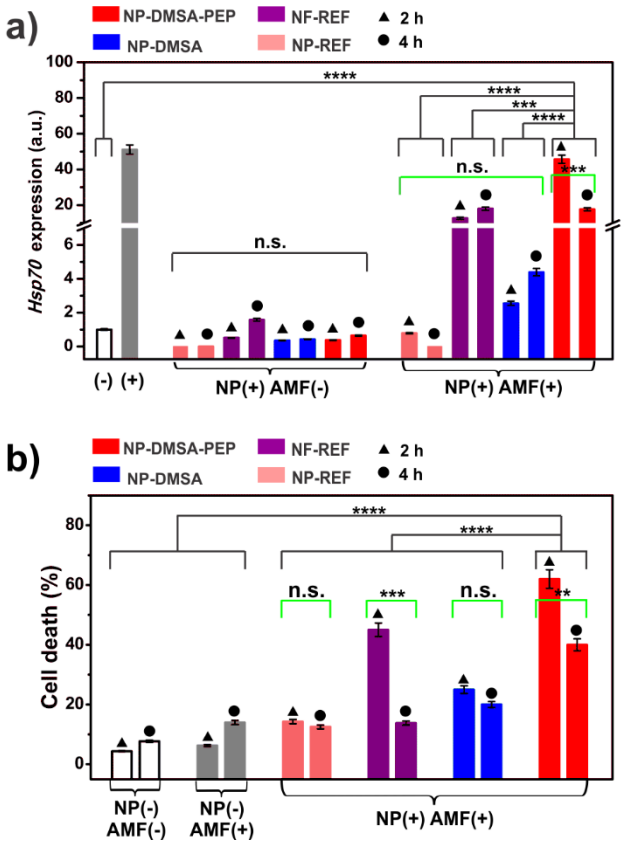

Figure 8. **Analysis of biological effect induced by MHT in U87MG cells.** (**a**) H*sp70* gene expression of U87MG cells heat shocked analyzed by qRT-PCR, 1h and after the treatment. Expression levels were compared with *hsp70* expression relative to cells incubated at 42°C for 30 min. Data were normalized using the $2^{-\Delta\Delta Ct}$ method and are shown as mean ± SD (n=3). (**b**) Trypan Blue staining was used to calculate the percentage of dead cells. (See color insert.) Asterisks indicate samples showing statistically significant differences between groups (black brackets) and times (green brackets) (*p < 0.05, **p < 0.01, ***p < 0.001 and ****p< 0.0001). Two- way ANOVA, Tukey's multiple comparisons test were made for both analyzes.

The second biological effect we have analyzed is whether AMF induced cell death in U87MG cells loaded with either NP-REF, NF-REF, NF-DMSA or NF-DMSA-PEP. NP-loaded U87MG cells have been exposed to an AMF for 1 h and stained with Trypan Blue immediately after the treatment. To determine the percentage of death cells, blue-stained cells (death) and non-stained cells (alive) have been counted (Figure 8b). In the case of the U87MG cells loaded with NF-DMSA-PEP, 62% and 40% cell death have been observed at 2 h and 4 h after incubation, while for NF-DMSA, 20% and 25% cell death has been detected

at 2 and 4 h. To evaluate if the applications of AMF affected the viability of U87MG cells, cells without NPs have been exposed to an AMF during 1 h. Under these conditions 6.25% and 13,95% cell death has been observed at 2 h and 4 h. In the case of NP-REF internalized in U87MG cells, no statistically significant difference in cell death has been observed after exposition to an AMF (14% at 2 h and 12.5% at 4 h), compared to U87MG cells without NPs exposed the AMF. In the cells loaded with NF-REF for 2 and 4 h, we have detected a 45% and 14% cell death, respectively. When the results obtained from the Trypan Blue and from the *hsp70* mRNA expression analysis have been compared, we have observed that in all the conditions where AMF induced *hsp70* mRNA expression in NPs-loaded cells, cell death induction has been observed, suggesting that the heat release by NPs after AMF expositions is, in part the cause of the observed cell death. Therefore, flower-like shape NPs induced the highest expression levels of *hsp70* and the highest cell death percentages, suggesting that nanoparticles shape could be a very important parameter to optimize the materials prepared as heat mediators for hyperthermia.

It has been described that cell-internalized iron oxide nanoparticles can generate ROS through the production of iron ions due to the Fenton reaction[54]. NPs-induced ROS generation can be further potentiated by increasing the temperature, which could be reached either by applying an extracellular or intracellular source of heat[51,55]. Because our previous results suggested that AMF is inducing intracellular hyperthermia in NPs-loaded U87MG cells, and AMF could be inducing oxidative stress directly by itself increasing the Fenton reaction on the surface of internalized NPs or indirectly by increasing intracellular temperature, we have decided, to study whether AMF exposure is inducing ROS in NPs-loaded U87MG cells. For this analysis, we have selected NF-DMSA-PEP because these NPs are the ones that induced

the highest *hsp70* expression levels and the highest cell death percentages after AMF exposition (Figure 8).

First, U87MG cells loaded with NF-DMSA-PEP for 2 or 4 h and exposed to AMF for 1 h have been stained immediately after hyperthermia treatment with DHR. Then, these cells have been counterstained with DAPI and mounted in Fluoromont-G. Finally, we have analyzed the ROS generation measuring the fluorescence intensity of the DHR. As we can see in Figure 9a, U87MG cells loaded with NF-DMSA-PEP for 2 or 4 h, and exposed to an AMF (named in the Figure 9a and b NF(+)AMF(+)) the fluorescence intensity increased dramatically compared to those cells without NF-DMSA-PEP (negative control: NF(-)AMF(-) and NF(-)AMF(+)) or the cells loaded with NF-DMSA-PEP for 2 and 4 h, but non exposed to AMF (named in the Figure 9a and b NF(+)AMF(-)). More insight of these results, quantitative image analysis (Figure 9b) has shown strong statistically significant differences (p<0.0001) between U87MG cells loaded with NF-DMSA-PEP (after 2 h incubation) and exposed to an AMF, and U87MG cells without NPs and exposed to an AMF treatment (named in the Figure 9 a and b NF(-)AMF(+)). It should be emphasized that NF-DMSA-PEP in U87MG cells does not generate oxidative stress by itself in comparison with the treatment condition (named in the Figure 9a and b NF(+)AMF(+)). However, DHR fluorescence intensity for U87MG cells incubated with NF-DMSA-PEP exposed to AMF were comparable to the one obtained inducing ROS in the same cells when incubated with 1 mM H_2O_2 (named in the Figure 9a and b NF(-)H_2O_2(+)) or 100 μL of a 0.05% Triton X-100 solution (named in the Figure 9a and b NF(-)Tx100(+)), that are the most used positive controls for oxidative stress induction. These results suggest that the AMF exposure to the internalized NF-DMSA-PEP induces a strong oxidative stress in U87MG cells.

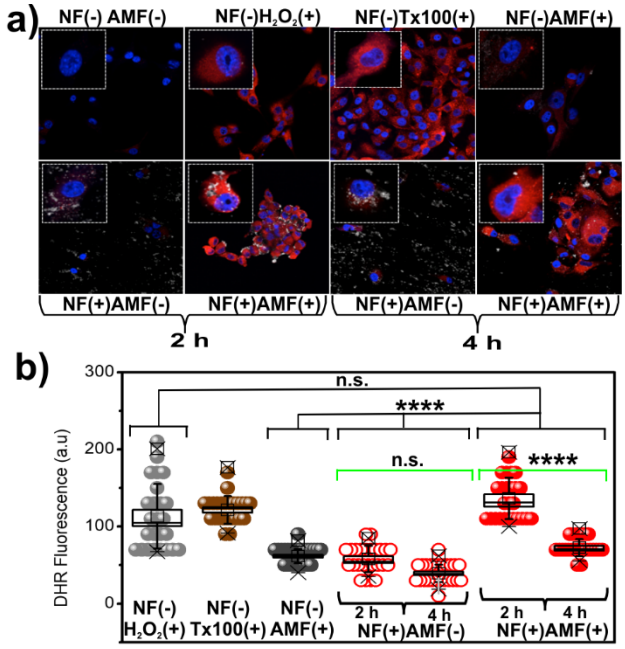

Figure 9. ROS induction in NF-DMSA-PEP-loaded U87MG cells after magnetic field application. (**a**) ROS generation observed by DHR fluorescence assay, (**b**) Quantitative image analysis of DHR fluorescence intensity. Besides NF-DMSA-PEP-loaded cells exposed to AMF (NF(+)AMF(+)), H_2O_2-treated (NF(-)H_2O_2(+)) and Triton X100-treated (NF(-)Tx(+)) cells were used as a positive control. As negative controls, cells without NPs nor AMF (NF(-)AMF(-)), cells without NPs and exposed to AMF (NF(-)AMF(+)), and cells loaded with NF-DMSA-PEP for 2 or 4 h, but non exposed to AMF (NF(+)AMF(-)) were used. Two-way ANOVA and Tukey's multiple comparisons test were made for DHR intensity analysis. (See color insert.). Asterisks indicate samples showing statistically significant differences in fluorescence intensity between groups (black brackets) and times (green brackets) (*$p < 0.05$, **$p < 0.01$, ***$p < 0.001$ and ****$p < 0.0001$).

Finally, we have analyzed if the AMF exposition of NF-DMSA-PEP-loaded U87MG cells triggers apoptosis as previously suggested for other magnetic nanoparticles[8,3,4]. We have used two approaches. First, we have used the TUNEL staining (Figure 10a and b) to evaluate the existence of possible DNA damage produced by the high oxidative stress induction observed in this U87MG cells loaded with NF-DMSA after AMF exposition. Second, we have quantified the activity of the caspase-3 protein (Figure 10c and d) as the activation of caspase-3 is a central event in the apoptosis triggering. Quantification of the number of cells positive from TUNEL images showed that a 7% of NF-DMSA-PEP-loaded U87MG cells are positive for this staining after exposition to the AMF (in the Figure 10b NF(+)AMF(+))) while U87MG cells without NPs exposed and non-exposed to AMF only shows 2% and 1% of

apoptotic cells. The differences observed between NF-DMSA-PEP-loaded in cells (for 2 h) and exposed to AMF (for 1 h) and the controls (cells with and without AMF) are not statistically significant.

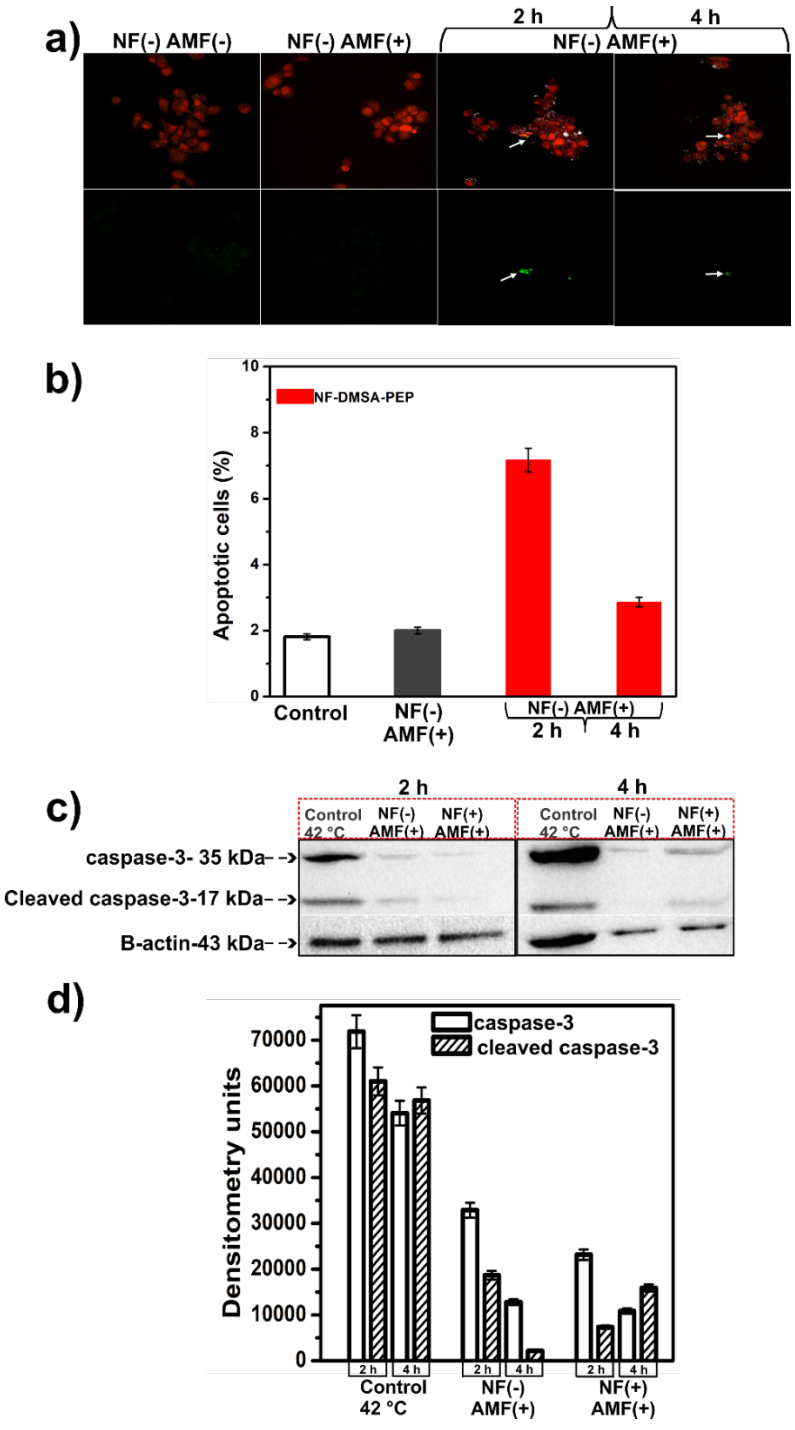

Figure 10. Determination of cell death induction in NF-DMSA-PEP-loaded U87MG cells after alternating magnetic field application. (**a**) TUNEL staining of U87MG cells and (**b**) quantification of the percentage of apoptotic cells based on TUNEL-positive cells. For TUNEL staining, Besides NF-DMSA-PEP-loaded cells exposed to AMF (NF(+)AMF(+)), cells without NPs nor AMF (NF(-)AMF(-)), and cells without NPs and exposed to AMF (NF(-)AMF(+)) were used as negative control. (**c**) Caspase-3 and cleaved caspase-3 expression detected by Western blot in U87MG cells exposed to AMF, and (**d**) Quantification of caspase-3 and cleaved caspase-3 levels. Besides NF-DMSA-PEP-loaded cells exposed to AMF (NF(+)AMF(+)), for Western blot analysis, cells incubated at 42ºC (30 min) were used as positive control. As negative control cells without NPs and exposed to AMF (NF(-)AMF(+)) were used. One-way ANOVA was performed for quantification of apoptotic cells.

These results agree with similar findings that describe hyperthermia as having no direct damaging effect on DNA[36]. However, given the complexity of identifying specific DNA damage after the treatment of magnetic hyperthermia we cannot discard it without further proof. In this sense, we have used the detection of active form of caspase-3 associated with MHT because this protease is an important marker of the cell's entry point into the apoptotic signaling pathway. For caspase-3 activity analysis, caspase-3 (35 KDa) and cleaved caspase-3 (17 kDa) have been analysed by Western blot immediately after AMF application (Figure 10c and d). As a positive control of caspase-3 activation we have incubated U87MG cells in a water bath at 42 ºC for 30 minutes. We have also checked whether incubation of U87MG cells with NF-DMSA-PEP (for 2 or 4 h) (named in the figure 10c NF(+)AMF(-)) induced any caspase-3 activity before exposition to the AMF. The results show (Figure 10c, d) similar caspase-3 activation between NF-DMSA-PEP-loaded U87MG cells exposed to AMF (named in the Figure 10c NF(+)AMF(+)) and NF-DMSA-PEP-loaded U87MG cells non-exposed to AMF suggesting that the AMF application does not induced apoptosis in NF-DMSA-PEP-loaded U87MG cells.

The hypothesis of the cell death mechanism observed in this work is shown in Figure 11. We conclude that the application of AMF to optimized NF-DMSA-PEP specifically delivered to endocytic vesicles evenly distributed in the cytoplasm of U87MG cells increases the temperature at the nanoparticle periphery which in turn enhances ROS production

through the Fenton reaction. Subsequently, several ROS mediated mechanisms induced the activation of *hsp70* proteins, cell membrane permeabilization and rupture and finally trigged cell death through non activation of caspase -3 apoptotic pathway.

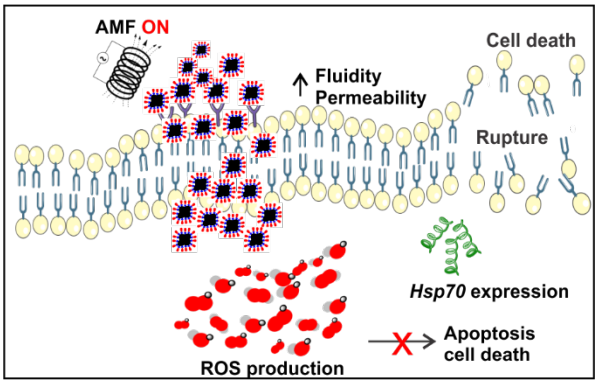

Figure 11. Hypothesis of the effects of MHT using NF-DMSA-PEP nanoparticles on U87MG cells.

CONCLUSIONS

Magnetic behavior of nanoparticles and consequently, the heating efficiency of the NPs under the action of an alternating magnetic field, are strongly affected by nanoparticle size, shape and aggregation. Particle size has been here chosen around 19 nm avoiding surface canting effects and Mn has been used as dopant to increase the saturation magnetization. In relation to the aggregation, although it is very often working in detriment of the heating efficiency, it is possible to control and even tune it through the right choice of the synthetic conditions and the surface modification in order to take advantage of it. This is the case of the so-called flower like nanoparticles (NF-DMSA) developed in this work, with important exchange interactions between the closely aggregated cores that exhibit continuity of the crystal lattice across the core's boundaries. In this way, we have ¨big¨ particles that exhibit

superparamagnetic behavior at room temperature, but they have a large effective anisotropy due to collective magnetic behavior. Dipolar interactions are however minimized by the presence of the peptide coating (NF-DMSA-PEP) that keeps the particles apart even after internalization in cells and increases the cell uptake up to six times respect to particles without coating.

Our results strongly suggest cycles of endocytosis/exocytosis of the cRGD-modified NPs that require the optimization of the cell incubation time to obtain the maximum uptake in the U87MG cell line. In U87MG cells incubated for 2 h and exposed to the AMF with NF-DMSA-PEP we have observed active *hsp70* transcription and a strong ROS induction, biological effects known to be consequence of intracellular heat induction. In addition, we have observed a high percentage of cell death induction (over 60%), which is not mediated by apoptosis induction, as shown by TUNEL and caspase-3 assays. Therefore, it can be concluded that when U87MG cells are loaded with the magnetically-improved NF-DMSA-PEP NPs and exposed to the right AMF conditions, this treatment induced intracellular magnetic hyperthermia under this condition, as it induces *hsp70* transcription and strong ROS production, that at the end causes cell death by mechanisms other than apoptosis induction. These results highlight the need for further research in optimization NPs with improved magnetic properties, to find the best time-window for NPs internalization in cells, and to find the best AMF application conditions to make the treatment more efficient.

Apart of that, intratumoral administration seems to be the best way of administration for these nanoparticles to guarantee its accumulation in the tumor and they will not end up somewhere else such as it was described for intravenous injected DMSA coated particles that accumulated in the lungs[57]. Furthermore, the peptide is expected to recognize specific

receptors on tumoral cells, that will favour the internalization of the nanoparticles on tumor cells and not in healthy cells. Several authors reported that cRGD has a high affinity with the $\alpha_v\beta_3$ integrin receptors overexpressed on angiogenic endothelial cells, as well as for tumor cells such as malignant glioma cells, breast cancer cells, bladder cancer cells and prostate cancer cells[32,17,58].

EXPERIMENTAL SECTION

Materials. Iron(III) acetylacetonate ($Fe(acac)_3$, 97%), manganese(II) acetylacetonate ($Mn(acac)_2$), oleic acid (≥99.0%, GC) and oleylamine (70.0%, technical grade) was obtained from Sigma-aldrich (México). Dimercaptosuccinic acid (DMSA) was purchased from Sigma Aldrich (Spain). Cyclo(-RGDfK) peptide (Purity: ≥ 98%) was obtained from MCE (New Jersey, USA). 1-Ethyl-3-(3-dimethylaminopropyl) carbodiimide hydrochloride (EDC·HCl) and N-hydroxysulfosuccinimide (sulfoNHS) (≥ 98%, HPLC grade) was purchased from Sigma- Aldrich (Spain). All organic solvents were of analytical grade or LC/MS grade.

Cells, Culture Medium and Biological Reagents. U87MG cells were obtained from the American Type Culture Collection (ATCC). Dulbecco's Modified Eagle Medium (DMEM, basic (1x), fetal bovine serum (FBS), L-glutamine, penicillin streptomycin and sodium pyruvate were supplied by Biowest. Micro BCA Protein Assay Kit, PrestoBlue Cell Viability Reagent (Invitrogen), Alexa Fluor 647-wheat germ agglutinin (Life Technologies) and Dihydrorhodamine 123 (DHR) were purchased by Thermo Fisher Scientific. TUNEL Assay Kit – FITC (ab66108) was obtained from abcam (Sapin). FITC-annexin V/propidium iodide (PI) and diamidino-2-phenylindole (DAPI) were purchased from SouthernBiotech. RNA

isolation kit, MultiScribe reverse transcription-based reaction kit and RNAse inhibitors (N8080119) were purchased from Thermo Fisher (Applied Biosystems). For the RT-qPCR, specific human *hsp70* and β-actin primers were supplied by Sigma-Aldrich. Primary antibodies for caspase-3 were obtained from Cell Signalling. RPN2106, Amersham ECL Western Blotting Detection Reagent was purchased by GE HealthCare.

Synthesis of NPs and Conjugation

Synthesis of flower-like $MnFe_2O_4$ nanoparticles (NF-OA): Flower-like $MnFe_2O_4$ nanoparticles were synthesized by thermal decompositon process according to a procedure previously described by Sun[59] with some modifications. $Fe(acac)_3$ (2 mmol), $Mn(acac)_2$ (1 mmol), oleic acid (4 mmol), oleylamine (4 mmol), without 1,2-hexadecanediol and 1-octadecene (15 mL) were mixed and magnetically stirred under a smooth nitrogen flow. The mixture was heated to 110 °C for 1 hour, then to 210 °C for two hours and finally, without stirred heated to reflux (280 °C) for another 1 hour. The black-brown mixture was cooled to room temperature by removing the heat source. Under ambient conditions, an ethanol excess was added to the mixture, and a black material was precipitated and separated via centrifugation (12000 rpm, 10min). The black product was dissolved in hexane, then precipitated with ethanol and centrifuged (12000 rpm, 10 min) to remove the solvent. This cycle was repeated 3 times giving a dark-brown powder, which was dispersed in hexane and kept at 4 °C.

For the sake of comparison, magnetite nanoparticles made by coprecipitation 12 nm in diameter (NP-REF) and nanoflowers made by hydrothermal synthesis in polyol media, 20 nm in diameter (NF-REF) were synthesized following previous reported processes[38,40].

Phase transfer of nanoparticles to the aqueous media (NF-DMSA). Following, the procedure reported in ref[59], 50 mg of nanoparticles were dispersed in toluene (20 mL) and the resulting black suspension was added to a solution of DMSA (90 mg) in dimethyl sulfoxide (5 mL). Then, the mixture was shaken in a laboratory tube rotator for 2 days. The resulting precipitate was washed with ethanol, sonicated, centrifuged (9000 rpm, 20 min) 3 times and then, redispersed in distilled water. The pH was adjusted with KOH from ca. 5 to 10. The dispersion was then placed in a cellulose membrane and dialyzed for 2 days in distilled water, to remove any excess of unreacted DMSA and any other small impurities that may be present in the dispersion unbound to the nanoparticles. Finally, the pH of the dispersion (ca. 5) was adjusted to 7 and the dispersion filtered through a filter with a pore size of 0.22 μm.

Conjugation of the cyclo(-RGDfK) peptide to the NPs (NF-DMSA-PEP). The peptide was covalently attached to the carboxyl groups present in the DMSA coating of the NPs by EDC/sulfoNHS chemistry following the procedure reported by Herranz[60]. In brief, 12 mg of 1-ethyl-3-(3-dimethylaminopropyl) carbodiimide hydrochloride (EDC) and 15 mg of N-hydroxysulfosuccinimide (sulfoNHS) were added to 5 mL of aqueous suspension of nanoparticles at concentration of [Fe =1mg/mL]. The mixture was stirred at room temperature for 30 min and posteriorly purified by ultrafiltration using 30 kDa cut-off filters. Filtered nanoparticles were diluted in buffer HEPES pH 8 to 1.8 mL, 1 mg of peptide was then added, and the mixture was stirred at room temperature for 60 min. Once this step was completed, the sample was purified by ultrafiltration and suspended in deionized water.

Determination of peptide conjugation efficiency. We used a colorimetric method based on Micro BCA Protein Assay Kit. In brief, 1 μL aliquots of NF-DMSA-PEP and NF-DMSA in 9 μL of MilliQ water were added in triplicate wells (96-well plate), followed by the

addition of 100 μL BCA Protein Assay Reagent, respectively. After 1 h incubation at 37 ºC, the absorption was measured using a microplate reader (Bio Rad, model 680) at 562 nm. The cRGD conjugation efficiency defined as the percentage in weight of peptide conjugated respect to the total added (CE%) was calculated as follows:

$$CE(\%) = \frac{ANP}{TA} \times 100 \qquad \textbf{(1)}$$

Where ANP is the amount of peptide conjugated on the NPs surface in grams and TA es the total amount of peptide added.

Characterization of powders and suspensions. Particle size, shape and distribution were evaluated in a conventional Transmission electron microscopy (TEM) images were obtained using JEOL JEM 1011 electron microscope, working at an acceleration voltage of 60 kV. High-resolution Transmission electron microscopy images (HRTEM), STEM (Scanning-Transmission) mode and energy-dispersive X-ray (EDX) were obtained by a Tecnai F30 microscope with an accelerating voltage of 300 keV, revealing the flower-like character of the particles. TEM and HRTEM samples were prepared by depositing 5 μL of dilute solution on a copper grid (200-mesh) and then drying at ambient temperature prior to analysis. The crystal structure of the sample was identified by X-Ray powder diffraction (XRD) performed in a Bruker D8 Advance diffractometer (with Cu Kα radiation, scan angle (10°–70°). The patterns were collected within 10º and 90º in 2θ. The concentration of Mn and Fe in aqueous dispersions and in cells were measured by elemental analysis with Inductively Coupled Plasma Atomic Emission Spectroscopy (ICP-OES) (Plasma Emission Spectrometer ICP PERKIN ELMER mod. OPTIMA 2100 DV, Perkin Elmer, Waltham, MA, USA). The samples (25 μL) were digested in aqua regia at 60 ºC overnight and diluted up a volume of 25 mL with deionized water. The surface chemistry and conjugation of different functional

moieties were elucidated from FTIR spectra using a Nicolet FT-IR 20SXC spectrometer recorded in the range of 400–4000 cm^{-1}. Samples were lyophilized for 24 h and thoroughly mixed and crushed with KBr to fabricate KBr pellets. The hydrodynamic diameters of nanoparticles and Zeta potential were measured with the dynamic light scattering (DLS) measurements (Nanosizer® ZS, Malvern, UK) at 25 °C. The Zeta potential was measured for aqueous samples using KOH and HNO_3 to vary the pH and KNO_3 (10^{-3} M) as the electrolyte. The suspensions (50 µl) were dried in a cotton piece and the magnetic behavior as a function of the magnetic field (5000 kA/m) and temperature was measured using a vibrating sample magnetometer (MagLab® VSM Oxford Instruments, UK). Zero field cool (ZFC)/field cool (FC) curves at 100 Oe were recorded.

Heating efficiency of the NPs in water under an AMF were analyzed in Eppendorf tubes containing 1mL of sample at 1 mg_{NPs}/mL concentration.

The equipment is a Five Celes MP 6kW device consisting of a generator with a frequency range between 100 and 400 kHz, connected to a cooling water circuit, a magnetic coil (magnetic field range: 0-600 Oe) molded solenoid with an internal diameter of 71 mm, a capacitor box Type ALU CU and an optic fiber sensor (measurement range -40 to 200ºC). The Eppendorf tube is located inside a polystyrene cylinder cavity, which guarantees a fixed position at the centre of the magnetic coil and thermal isolation. The temperature change was measured as a function of time (dT/dt) and the initial linear slope (t = 30 s) was used to evaluate the heating efficiency in terms of SAR, power dissipation per unit mass of element, i.e. iron plus manganese (W g^{-1}) using the following formula:

$$SAR = \frac{\Delta T}{\Delta t}\frac{C}{m_{Fe+Mn}} \qquad \textbf{(2)}$$

where the C is the specific heat capacity of the liquid solvent, the solvent in our experiment is water which can be recognized of C water 4185 J L^{-1} K^{-1}, and m is the iron and manganese content per unit mass of the material solutions.

Cell culture. Human glioblastoma cancer cells were cultured in Dulbecco's modified Eagle's medium (DMEM) supplemented with 10% fetal bovine serum (FBS), L-glutamine (2mM), penicillin streptomycin (10U/mL) and sodium pyruvate (1mM) and maintained at 37 °C with 5% CO_2 and 90% relative humidity.

Viability assay/ Cell death analysis before MHT. Cell viability was evaluated by three methods: PrestoBlue assays, Tunel and FITC-annexin V/propidium iodide staining. In the PrestoBlue assay, U87MG cells were cultured ($1x10^4$ cells/well) in a 96-well plate with 6 different concentrations of NF-DMSA and NF-DMSA-PEP nanoparticles (0, 20, 40, 60, 80, 100 μg/mL) for 24 h and PrestoBlue was added to each well, incubated for 4h and the fluorescence (Ex/Em = 530/590 nm) was measured on a TECAN Infinite 200 Pro Fluorometer. Cell survival was expressed as the percentage of fluorescence of MNP-treated cells compared to untreated cells. For Tunel staining, U87MG cells were seeded at a concentration of 1×10^5 cells/ml in 24-well plates and incubated with two different concentrations of NF-DMSA and NF-DMSA-PEP nanoparticles (60 and 100 μg/mL) for 2 and 4 h. The number of total and Tunel positive cells were analysed using Image J (NIH, USA) Software. Finally, cell survival was analyzed for FITC-annexin V/propidium iodide staining (Ex/Em = 495/519nm).

Cellular Uptake, **cellular and subcellular localization.** Iron Quantification by ICP-OES. The cells were seeded into a 6-well plate with a density of $2x10^4$ cells per well (24 h, 37 ºC). Then, NF-DMSA and NF-DMSA-PEP samples with different concentration (0, 40, 60,100

μg/mL) were added into the plate at different time intervals (0, 2, and 4 h). After incubation, the cells were washed three times with PBS to remove non-internalized MNP, harvested and counted in a Neubauer chamber. The samples were digested in HNO_3 (1 mL) and H_2O_2 (1 mL) for 1h at 90°C. The amount of iron per cell was measured by ICP-OES (Perkin Elmer-2400). Visualization by Confocal and Transmission Electron Microscopy. Different microscopy techniques were used to determine NPs subcellular location. For dark-field confocal microscopy, Alexa Fluor 647-wheat germ agglutinin was added during the last 15 min. Cells were then washed, fixed with PFA 4% (15 min), counterstained with DAPI and mounted in Fluoromont-G. Finally, they were observed in a Confocal Laser Scanning Microscope Leica TCS SP5 (Leica Microsystems) using a 63x/1.4 NA oil immersion objective. For TEM microscopy, $2x10^6$ cells were seeded on petri dishes for 24 h. After that, 60 μg/mL of each NPs in DMEM were added to the cells and left for 0, 2, 4 and 24 h. Non-internalized nanoparticles were removed washing with PBS. Cells were subsequently fixed at RT in 2 % glutaraldehyde, 1 % tanic acid in 0.4 M HEPES at pH 7.2. The cells were washed and suspended in HEPES buffer, post-fixed with 1% osmium tetroxide (1 h) and 2% uranyl acetate (30 min; both at 4 °C), dehydrated with a series of acetone solutions and gradually infiltrated with Epon resin. The resin was allowed to polymerize (60 °C, 48 h), and ultrathin sections (60–70 nm) were obtained with a diamond knife mounted on a Leica EM UC6 ultramicrotome. Sections were supported on a formvar/carbon-coated gold grid and observed using a JEOL-1011. Images were acquired at different magnifications with a JEOL JEM 1011 transmission electron microscope with Gatan ES1000Ww camera.

MHT of U87MG cells: For cell treatment under an AMF, $1x10^6$ U87MG cells were seeded in petri dishes (Falcon, 35 x 10 mm), incubated for 24 h with NPs (NP+) or without NPs (NP-

), washed 3-times with culture media to eliminate the non-internalized NPs, and finally exposed to AMF for 1 h (H = 47 kA/m, f = 96 kHz). The experiments were carried out in duplicate under four different conditions: U87MG cells incubated for 2 and 4 h at 37 ºC (the temperature was controlled throughout the treatment by a thermal probe) with 60 μg/ml of NPs and exposed to AMF; cells incubated with NPs and non-exposed to AMF; cells exposed to AMF without NPs; and control cells (without CO_2 at 37 ºC for the same time of the treatment). The experiment was carried out for the following samples: NF-DMSA-PEP, NF-DMSA, NF-REF and NP-REF.

Cell death analysis after MHT: Trypan blue assay. After MHT, NPs-loaded cells (NF-DMSA-PEP or NF-DMSA or NF-REF or NP-REF) and cells used as controls, i.e. cells incubated without CO_2 at 37 ºC for 1 h and cells exposed to AMF for 1 h without NPs, were harvested and resuspended in DMEM. 10 μL 0.4% trypan blue solution were added to 10 μL of cells suspension. Blue-stained cells (dead) and non-stained cells (live) were counted immediately after mixing using a Neubauer chamber, and the percentage of dead blue cells determined from at least three independent experiments done in triplicates.

***Hsp70* gene expression.** After hyperthermia treatment cells were kept in the incubator for 1 h in standard culture conditions to let the transcription machinery work. Then RNA was extracted from cells using the PureLink RNA Mini Kit following manufacturer's instructions. RNA concentration was determined by absorbance measurements at 260 nm in a NanoDrop 1000 spectrophotometer (Thermo Scientific) and 40 ng RNA/sample were used to generated cDNA using a MultiScribe reverse transcription-based reaction kit in the presence of a RNAse inhibitors in a MyCycler thermocycler (Bio-Rad; 25 °C-10 min, 37 °C-2 h, 85 °C-5 min, 4 ºC). The induction of HSPA1B (Heat shock protein family A (*hsp70*) member 1B)

expression was measured by quantitative RT-PCR. For the RT-qPCR we used specific human *hsp70* and β-actin primers (F: CCTATGTCATTTCTGGTTCAG and R: TTTAAAGGGAACGAAACACC from human HSPA 1B and F: GACGACATGGAGAAAATCTG and R: ATGATCTGGGTCATCTTCTC from human β-actin). Data were acquired using the SDS 2.4 software, and analyzed with the Expression Suite 1.1 software (both from Applied Biosystems), according to the $2^{-\Delta\Delta C_t}$ method[61].

Tunel assay. After AMF treatment, apoptosis was analyzed using the Tunel assay, as already describe above.

Western blot. Immediately after the hyperthermia treatment, the U87MG cells were lysed with Triton X-100/EDTA solution containing a protease inhibitors cocktail (leupeptin, 1 μg/mL; NaF, 5 nM; sodium orthovanadate, 1 mM; phenylmethylsulfonyl fluoride (PMSF), 1 mM; EDTA, 0.5 mM; aprotinin, 1 μg/mL and okadaic acid, 1 μg/mL) (45 min, 4 °C). Total protein concentration in the cell extract was quantified using Micro BCA protein assay kit. Equal amounts of protein from lysates (40 μg/well) were loaded onto gels and resolved by SDS-PAGE (10%). Samples were transferred to 0.2 μm PVDF membranes (BioRad), which were blocked with Tris-buffered saline (TBS)/0.05% Tween 20/5% bovine serum albumin (BSA) (room temperature, 30 min). For immunoblotting, we used specific primary antibodies for caspase-3 and β-actin. After incubation with the appropriate secondary antibodies conjugated with horseradish peroxidase-conjugated (Dako), protein bands were visualized using ECL Western Blotting Detection Reagent and developed on A-Plus Medical film (Konica Minolta). Antibody specific bands corresponding to caspase-3 expected molecular weight have been quantified used the ImageJ software.

Analysis of ROS generation. Immediately after AMF treatment, ROS generation was analyze using Dihydrorhodamine 123 (DHR) assay in AMF expose U87MG cells. First, cells were incubated for 20 min with DHR (10 μM). Then cells were washed with PBS (1X) at RT, fixed with PFA 4 % (15 min), counterstained with DAPI for 10 minutes and mounted in Fluoromont-G. Dihydrorhodamine 123 is an uncharged and non-fluorescent ROS indicator that can passively diffuse across membranes where it is oxidized to cationic rhodamine 123 that localizes in the mitochondria and emits red fluorescence (Ex/Em = 500/563nm). As positive control of oxidative stress induction in U87MG cells, cells were incubated with 1mM H_2O_2 for 30 minutes. To asses if any of the observed effects was possibly due to membrane permeabilization we treat the cells with 100 μL of a 0.05 % Triton X-100 solution for 10 minutes. As negative control DHR was measured the intensity of fluorescence in cells incubated with NF-DMSA-PEP and non-exposed to AMF and cells exposed to AMF without NPs. For DHR quantification we used Image J software using the intensity measurement.

Statistical analysis: All data are presented as mean ± standard deviation (SD). One-way and Two-way analysis of variance (ANOVA) and Tukey test were applied to calculate the differences between the values. Values of $p < 0.05$ were considered statistically significant. The levels of significance are presented as * ($p < 0.05$), ** ($p < 0.01$), *** ($p < 0.001$) and ****($p < 0.0001$).

***Supporting Information**

ATR spectra of Cyclo(-RGDfK) peptide; estimation of the number of Cyclo(-RGDfK) peptide molecules on NF-DMSA nanoparticles surface; hysteresis loops recorded at 5 K and ZFC-FC curves at 290 K for NF-DMSA and NF-DMSA-PEP nanoparticles; table with the values of magnetic properties of NF-DMSA and NF-DMSA-PEP nanoparticles at 5 and 290 K; transmission electron microscope (TEM) images of the reference samples (NF-REF and

NP-REF); heating curves of NF-DMSA-PEP in water and NF-DMSA-PEP in a water/glycerol mixture (50/50, v/v); FITC-annexin V/propidium iodide analysis after incubation with NF-DMSA or NF-DMSA-PEP at 24 h (0 -100 μg Fe/mL concentration of NPs) in U87MG cells; Uptake kinetics for NF-DMSA and NF-DMSA-PEP nanoparticles (0, 2, 4, 8, 24 h) at different concentration of NPs; quantification of iron content in the supernatant before (SN1) and after (SN2) MHT with NF-DMSA-PEP loaded U87MG cells at 2 an 4 h.

Conflict of Interest

The authors declare no competing financial interest.

Acknowledgement

This work was supported by the Spanish Ministerio de Ciencia, Innovación y Universidades, under the following projects: Project MAT2017-88148-R, SAF-2017-82223-R, PIE-201760E007 and Nanobioap cluster of excellence under project MAT2016-81955-REDT. Portilla receives a predoctoral FPU grant (FPU15/06170) from the same Ministry. S. Del Sol acknowledges the economic support by CONACyT and Instituto Politécnico Nacional SIP 20180252 (México). The authors thank the CNB confocal microscopy facility, the CNB flow cytometry facility, and CNB TEM facility, for their technical support. L.G. acknowledges financial support from the Ramón y Cajal subprogram (RYC-2014-15512). Authors would like to acknowledge the Advanced Microscopy Laboratory (INA-Universidad de Zaragoza) for access to their instrumentation and expertise.

References

(1) Blanco-Andujar, C.; Walter, A.; Cotin, G.; Bordeianu, C.; Mertz, D.; Felder-Flesch, D.; Begin-Colin, S. Design of Iron Oxide-Based Nanoparticles for Mri and Magnetic Hyperthermia. *Nanomedicine (Lond)* **2016,** *11*, 1889-1910.
(2) Tsiapa, I.; Efthimiadou, E. K.; Fragogeorgi, E.; Loudos, G.; Varvarigou, A. D.; Bouziotis, P.; Kordas, G. C.; Mihailidis, D.; Nikiforidis, G. C.; Xanthopoulos, S. 99mtc-Labeled Aminosilane-Coated Iron Oxide Nanoparticles for Molecular Imaging of Avβ3-Mediated Tumor Expression and Feasibility for Hyperthermia Treatment. *J. Colloid Interface Sci* **2014,** *433*, 163-175.
(3) Cellai, F.; Munnia, A.; Viti, J.; Doumett, S.; Ravagli, C.; Ceni, E.; Mello, T.; Polvani, S.; Giese, R. W.; Baldi, G.; Galli, A.; Peluso, M. E. M. Magnetic Hyperthermia and Oxidative Damage to DNA of Human Hepatocarcinoma Cells. *Int J Mol Sci* **2017,** *18*, 939.
(4) Ludwig, R.; Teran, F. J.; Teichgraeber, U.; Hilger, I. Nanoparticle-Based Hyperthermia Distinctly Impacts Production of Ros, Expression of Ki-67, Top2a, and Tpx2, and Induction of Apoptosis in Pancreatic Cancer. *Int J Nanomedicine* **2017,** *12*, 1009-1018.
(5) van den Tempel, N.; Horsman, M. R.; Kanaar, R. Improving Efficacy of Hyperthermia in Oncology by Exploiting Biological Mechanisms. *Int J Hyperther* **2016,** *32*, 446-454.
(6) Zhang, J.; Dewilde, A. H.; Chinn, P.; Foreman, A.; Barry, S.; Kanne, D.; Braunhut, S. J. Herceptin-Directed Nanoparticles Activated by an Alternating Magnetic Field Selectively Kill Her-2 Positive Human Breast Cells in Vitro Via Hyperthermia. *Int J Hyperther* **2011,** *27*, 682-697.
(7) Evans, S. S.; Repasky, E. A.; Fisher, D. T. Fever and the Thermal Regulation of Immunity: The Immune System Feels the Heat. *Nat Rev Immunol* **2015,** *15*, 335-349.
(8) Clerc, P.; Jeanjean, P.; Hallali, N.; Gougeon, M.; Pipy, B.; Carrey, J.; Fourmy, D.; Gigoux, V. Targeted Magnetic Intra-Lysosomal Hyperthermia Produces Lysosomal Reactive Oxygen Species and Causes Caspase-1 Dependent Cell Death. *J Control Release* **2018,** *270*, 120-134.
(9) Lee, J. H.; Jang, J. T.; Choi, J. S.; Moon, S. H.; Noh, S. H.; Kim, J. W.; Kim, J. G.; Kim, I. S.; Park, K. I.; Cheon, J. Exchange-Coupled Magnetic Nanoparticles for Efficient Heat Induction. *Nat Nanotechnol* **2011,** *6*, 418-422.
(10) Dennis, C. L.; Jackson, A. J.; Borchers, J. A.; Hoopes, P. J.; Strawbridge, R.; Foreman, A. R.; van Lierop, J.; Gruttner, C.; Ivkov, R. Nearly Complete Regression of Tumors Via Collective Behavior of Magnetic Nanoparticles in Hyperthermia. *Nanotechnology* **2009,** *20*, 395103.
(11) Kossatz, S.; Grandke, J.; Couleaud, P.; Latorre, A.; Aires, A.; Crosbie-Staunton, K.; Ludwig, R.; Dahring, H.; Ettelt, V.; Lazaro-Carrillo, A.; Calero, M.; Sader, M.; Courty, J.; Volkov, Y.; Prina-Mello, A.; Villanueva, A.; Somoza, A.; Cortajarena, A. L.; Miranda, R.; Hilger, I. Efficient Treatment of Breast Cancer Xenografts with Multifunctionalized Iron Oxide Nanoparticles Combining Magnetic Hyperthermia and Anti-Cancer Drug Delivery. *Breast Cancer Res* **2015,** *17*, 66.

(12) Espinosa, A.; Kolosnjaj-Tabi, J.; Abou-Hassan, A.; Sangnier, A. P.; Curcio, A.; Silva, A. K. A.; Di Corato, R.; Neveu, S.; Pellegrino, T.; Liz-Marzan, L. M.; Wilhelm, C. Magnetic (Hyper)Thermia or Photothermia? Progressive Comparison of Iron Oxide and Gold Nanoparticles Heating in Water, in Cells, and in Vivo. *Adv Funct Mater* **2018,** *28*, 1803660.
(13) Dennis, C. L.; Ivkov, R. J. I. J. o. H. Physics of Heat Generation Using Magnetic Nanoparticles for Hyperthermia. **2013,** *29*, 715-729.
(14) Hugounenq, P.; Levy, M.; Alloyeau, D.; Lartigue, L.; Dubois, E.; Cabuil, V.; Ricolleau, C.; Roux, S.; Wilhelm, C.; Gazeau, F.; Bazzi, R. Iron Oxide Monocrystalline Nanoflowers for Highly Efficient Magnetic Hyperthermia. *J Phys Chem C* **2012,** *116*, 15702-15712.
(15) Guardia, P.; Di Corato, R.; Lartigue, L.; Wilhelm, C.; Espinosa, A.; Garcia-Hernandez, M.; Gazeau, F.; Manna, L.; Pellegrino, T. Water-Soluble Iron Oxide Nanocubes with High Values of Specific Absorption Rate for Cancer Cell Hyperthermia Treatment. *ACS Nano* **2012,** *6*, 3080-3091.
(16) Di Corato, R.; Espinosa, A.; Lartigue, L.; Tharaud, M.; Chat, S.; Pellegrino, T.; Menager, C.; Gazeau, F.; Wilhelm, C. Magnetic Hyperthermia Efficiency in the Cellular Environment for Different Nanoparticle Designs. *Biomaterials* **2014,** *35*, 6400-6411.
(17) Sangnier, A. P.; Preveral, S.; Curcio, A.; Silva, A. K.; Lefèvre, C. T.; Pignol, D.; Lalatonne, Y.; Wilhelm, C. Targeted Thermal Therapy with Genetically Engineered Magnetite Magnetosomes@ Rgd: Photothermia Is Far More Efficient Than Magnetic Hyperthermia. *J. Control. Release* **2018,** *279*, 271-281.
(18) Etheridge, M. L.; Hurley, K. R.; Zhang, J.; Jeon, S.; Ring, H. L.; Hogan, C.; Haynes, C. L.; Garwood, M.; Bischof, J. C. Accounting for Biological Aggregation in Heating and Imaging of Magnetic Nanoparticles. *Technology (Singap World Sci)* **2014,** *2*, 214-228.
(19) Chen, W. H.; Luo, G. F.; Zhang, X. Z. Recent Advances in Subcellular Targeted Cancer Therapy Based on Functional Materials. *Adv Mater* **2019,** *31*, e1802725.
(20) Mejías, R.; Hernández Flores, P.; Talelli, M.; Tajada-Herráiz, J. L.; Brollo, M. E.; Portilla, Y.; Morales, M. P.; Barber, D. F. Cell-Promoted Nanoparticle Aggregation Decreases Nanoparticle-Induced Hyperthermia under an Alternating Magnetic Field Independently of Nanoparticle Coating, Core Size, and Subcellular Localization. *ACS Appl. Mater. Interfaces* **2018,** *11*, 340-355.
(21) Dennis, C. L.; Jackson, A. J.; Borchers, J. A.; Ivkov, R.; Foreman, A. R.; Lau, J. W.; Goernitz, E.; Gruettner, C. The Influence of Collective Behavior on the Magnetic and Heating Properties of Iron Oxide Nanoparticles. *J Appl Phys* **2008,** *103*, 07A319.
(22) Creixell, M.; Bohorquez, A. C.; Torres-Lugo, M.; Rinaldi, C. Egfr-Targeted Magnetic Nanoparticle Heaters Kill Cancer Cells without a Perceptible Temperature Rise. *Acs Nano* **2011,** *5*, 7124-7129.
(23) Dias, J. T.; Moros, M.; Del Pino, P.; Rivera, S.; Grazu, V.; de la Fuente, J. M. DNA as a Molecular Local Thermal Probe for the Analysis of Magnetic Hyperthermia. *Angew Chem Int Ed Engl* **2013,** *52*, 11526-11529.

(24) Sadhukha, T.; Niu, L.; Wiedmann, T. S.; Panyam, J. Effective Elimination of Cancer Stem Cells by Magnetic Hyperthermia. *Mol Pharm* **2013,** *10*, 1432-1441.
(25) Kim, D. H.; Rozhkova, E. A.; Ulasov, I. V.; Bader, S. D.; Rajh, T.; Lesniak, M. S.; Novosad, V. Biofunctionalized Magnetic-Vortex Microdiscs for Targeted Cancer-Cell Destruction. *Nat Mater* **2010,** *9*, 165-171.
(26) Salas, G.; Veintemillas-Verdaguer, S.; Morales, M. D. Relationship between Physico-Chemical Properties of Magnetic Fluids and Their Heating Capacity. *Int J Hyperther* **2013,** *29*, 768-776.
(27) Yang, L. J.; Ma, L. C.; Xin, J. Y.; Li, A.; Sun, C. J.; Wei, R. X.; Ren, B. W.; Chen, Z.; Lin, H. Y.; Gao, J. H. Composition Tunable Manganese Ferrite Nanoparticles for Optimized T-2 Contrast Ability. *Chem Mater* **2017,** *29*, 3038-3047.
(28) Liu, X. L.; Ng, C. T.; Chandrasekharan, P.; Yang, H. T.; Zhao, L. Y.; Peng, E.; Lv, Y. B.; Xiao, W.; Fang, J.; Yi, J. B. Synthesis of Ferromagnetic Fe0. 6mn0. 4o Nanoflowers as a New Class of Magnetic Theranostic Platform for in Vivo T1-T2 Dual-Mode Magnetic Resonance Imaging and Magnetic Hyperthermia Therapy. *Adv Healthc Mater* **2016,** *5*, 2092-2104.
(29) Hemery, G.; Genevois, C.; Couillaud, F.; Lacomme, S.; Gontier, E.; Ibarboure, E.; Lecommandoux, S.; Garanger, E.; Sandre, O. Monocore Vs. Multicore Magnetic Iron Oxide Nanoparticles: Uptake by Glioblastoma Cells and Efficiency for Magnetic Hyperthermia. *Mol Syst Des Eng* **2017,** *2*, 629-639.
(30) Hu, Y.; Li, J.; Yang, J.; Wei, P.; Luo, Y.; Ding, L.; Sun, W.; Zhang, G.; Shi, X.; Shen, M. Facile Synthesis of Rgd Peptide-Modified Iron Oxide Nanoparticles with Ultrahigh Relaxivity for Targeted Mr Imaging of Tumors. *Biomater Sci* **2015,** *3*, 721-732.
(31) Danhier, F.; Le Breton, A.; Preat, V. Rgd-Based Strategies to Target Alpha(V) Beta(3) Integrin in Cancer Therapy and Diagnosis. *Mol Pharm* **2012,** *9*, 2961-2973.
(32) Xie, J.; Chen, K.; Lee, H.-Y.; Xu, C.; Hsu, A. R.; Peng, S.; Chen, X.; Sun, S. Ultrasmall C (Rgdyk)-Coated Fe3o4 Nanoparticles and Their Specific Targeting to Integrin Avβ3-Rich Tumor Cells. *J. Am. Chem. Soc* **2008,** *130*, 7542-7543.
(33) Luo, Y.; Yang, J.; Yan, Y.; Li, J. C.; Shen, M. W.; Zhang, G. X.; Mignani, S.; Shi, X. Y. Rgd- Functionalized Ultrasmall Iron Oxide Nanoparticles for Targeted T-1-Weighted Mr Imaging of Gliomas. *Nanoscale* **2015,** *7*, 14538-14546.
(34) Passemard, S.; Staedler, D.; Ucnova, L.; Schneiter, G. S.; Kong, P.; Bonacina, L.; Juillerat-Jeanneret, L.; Gerber-Lemaire, S. Convenient Synthesis of Heterobifunctional Poly(Ethylene Glycol) Suitable for the Functionalization of Iron Oxide Nanoparticles for Biomedical Applications. *Bioorg Med Chem Lett* **2013,** *23*, 5006-5010.
(35) Cui, Y.; Song, X.; Li, S.; He, B.; Yuan, L.; Dai, W.; Zhang, H.; Wang, X.; Yang, B.; Zhang, Q. The Impact of Receptor Recycling on the Exocytosis of Avβ3 Integrin Targeted Gold Nanoparticles. *Oncotarget* **2017,** *8*, 38618.
(36) Zahraei, M.; Marciello, M.; Lazaro-Carrillo, A.; Villanueva, A.; Herranz, F.; Talelli, M.; Costo, R.; Monshi, A.; Shahbazi-Gahrouei, D.; Amirnasr, M.; Behdadfar, B.; Morales, M. P.

Versatile Theranostics Agents Designed by Coating Ferrite Nanoparticles with Biocompatible Polymers. *Nanotechnology* **2016,** *27*, 255702.
(37) Ruta, S.; Chantrell, R.; Hovorka, O. Unified Model of Hyperthermia Via Hysteresis Heating in Systems of Interacting Magnetic Nanoparticles. *Sci Rep* **2015,** *5*, 9090.
(38) Massart, R. Preparation of Aqueous Magnetic Liquids in Alkaline and Acidic Media. *IEEE Trans. Magn* **1981,** *17*, 1247-1248.
(39) Salas, G.; Casado, C.; Teran, F. J.; Miranda, R.; Serna, C. J.; Morales, M. P. Controlled Synthesis of Uniform Magnetite Nanocrystals with High-Quality Properties for Biomedical Applications. *J Mater Chem* **2012,** *22*, 21065-21075.
(40) Gavilan, H.; Sanchez, E. H.; Broll, M. E. F.; Asin, L.; Moerner, K. K.; Frandsen, C.; Lazaro, F. J.; Serna, C. J.; Veintemillas-Verdague, S.; Morales, M. P.; Gutierrez, L. Formation Mechanism of Maghemite Nanoflowers Synthesized by a Polyol-Mediated Process. *Acs Omega* **2017,** *2*, 7172-7184.
(41) Hergt, R.; Dutz, S. Magnetic Particle Hyperthermia-Biophysical Limitations of a Visionary Tumour Therapy. *J. Magn. Magn. Mater* **2007,** *311*, 187-192.
(42) Branquinho, L. C.; Carriao, M. S.; Costa, A. S.; Zufelato, N.; Sousa, M. H.; Miotto, R.; Ivkov, R.; Bakuzis, A. F. Effect of Magnetic Dipolar Interactions on Nanoparticle Heating Efficiency: Implications for Cancer Hyperthermia. *Sci Rep* **2013,** *3*, 2887.
(43) Tomitaka, A.; Ueda, K.; Yamada, T.; Takemura, Y. Heat Dissipation and Magnetic Properties of Surface-Coated Fe3o4 Nanoparticles for Biomedical Applications. *J. Magn. Magn. Mater* **2012,** *324*, 3437-3442.
(44) Serantes, D.; Simeonidis, K.; Angelakeris, M.; Chubykalo-Fesenko, O.; Marciello, M.; Morales, M. D.; Baldomir, D.; Martinez-Boubeta, C. Multiplying Magnetic Hyperthermia Response by Nanoparticle Assembling. *J Phys Chem* **2014,** *118*, 5927-5934.
(45) Wildeboer, R. R.; Southern, P.; Pankhurst, Q. A. On the Reliable Measurement of Specific Absorption Rates and Intrinsic Loss Parameters in Magnetic Hyperthermia Materials. *J Phys D Appl Phys* **2014,** *47*, 495003.
(46) Kou, L.; Sun, J.; Zhai, Y.; He, Z. The Endocytosis and Intracellular Fate of Nanomedicines: Implication for Rational Design. *J Asian Journal of Pharmaceutical Sciences* **2013,** *8*, 1-10.
(47) Mayor, S.; Pagano, R. E. Pathways of Clathrin-Independent Endocytosis. *Nat Rev Mol Cell Biol* **2007,** *8*, 603-612.
(48) Oh, N.; Park, J. H. Endocytosis and Exocytosis of Nanoparticles in Mammalian Cells. *Int J Nanomedicine* **2014,** *9 Suppl 1*, 51-63.
(49) Canton, I.; Battaglia, G. Endocytosis at the Nanoscale. *Chem Soc Rev* **2012,** *41*, 2718-2739.
(50) Paul, N. R.; Jacquemet, G.; Caswell, P. T. Endocytic Trafficking of Integrins in Cell Migration. *Curr Biol* **2015,** *25*, R1092-1105.
(51) Moros, M.; Ambrosone, A.; Stepien, G.; Fabozzi, F.; Marchesano, V.; Castaldi, A.; Tino, A.; de la Fuente, J. M.; Tortiglione, C. Deciphering Intracellular Events Triggered by

Mild Magnetic Hyperthermia in Vitro and in Vivo. *Nanomedicine (Lond)* **2015,** *10*, 2167-2183.
(52) Qu, Y.; Li, J.; Ren, J.; Leng, J.; Lin, C.; Shi, D. Enhanced Synergism of Thermo-Chemotherapy by Combining Highly Efficient Magnetic Hyperthermia with Magnetothermally-Facilitated Drug Release. *Nanoscale* **2014,** *6*, 12408-12413.
(53) Wang, B.; Yin, J.-J.; Zhou, X.; Kurash, I.; Chai, Z.; Zhao, Y.; Feng, W. Physicochemical Origin for Free Radical Generation of Iron Oxide Nanoparticles in Biomicroenvironment: Catalytic Activities Mediated by Surface Chemical States. *J. Phys. Chem. C* **2012,** *117*, 383-392.
(54) Kim, J.; Cho, H. R.; Jeon, H.; Kim, D.; Song, C.; Lee, N.; Choi, S. H.; Hyeon, T. Continuous O2-Evolving Mnfe2o4 Nanoparticle-Anchored Mesoporous Silica Nanoparticles for Efficient Photodynamic Therapy in Hypoxic Cancer. *J Am Chem Soc* **2017,** *139*, 10992-10995.
(55) Sanz, B.; Calatayud, M. P.; Torres, T. E.; Fanarraga, M. L.; Ibarra, M. R.; Goya, G. F. Magnetic Hyperthermia Enhances Cell Toxicity with Respect to Exogenous Heating. *Biomaterials* **2017,** *114*, 62-70.
(56) Oei, A. L.; Vriend, L. E. M.; Crezee, J.; Franken, N. A. P.; Krawczyk, P. M. Effects of Hyperthermia on DNA Repair Pathways: One Treatment to Inhibit Them All. *Radiation Oncology* **2015,** *10*, 165.
(57) Mejías, R.; Gutiérrez, L.; Salas, G.; Pérez-Yagüe, S.; Zotes, T. M.; Lázaro, F. J.; Morales, M. P.; Barber, D. F. Long Term Biotransformation and Toxicity of Dimercaptosuccinic Acid-Coated Magnetic Nanoparticles Support Their Use in Biomedical Applications. *J. Control. Release* **2013,** *171*, 225-233.
(58) Song, Y. S.; Park, H. S.; Lee, B. C.; Jung, J. H.; Lee, H.-Y.; Kim, S. E. Imaging of Integrin Avβ3 Expression in Lung Cancers and Brain Tumors Using Single-Photon Emission Computed Tomography with a Novel Radiotracer 99mtc-Ida-D-[C (Rgdfk)] 2. *J. Cancer Biotherapy Radiopharmaceuticals* **2017,** *32*, 288-296.
(59) Sun, S.; Zeng, H.; Robinson, D. B.; Raoux, S.; Rice, P. M.; Wang, S. X.; Li, G. Monodisperse Mfe2o4 (M = Fe, Co, Mn) Nanoparticles. *J Am Chem Soc* **2004,** *126*, 273-279.
(60) Herranz, F.; Morales, M. P.; Roca, A. G.; Vilar, R.; Ruiz-Cabello, J. A New Method for the Aqueous Functionalization of Superparamagnetic Fe2o3 Nanoparticles. *Contrast Media Mol Imaging* **2008,** *3*, 215-222.
(61) Livak, K. J.; Schmittgen, T. D. Analysis of Relative Gene Expression Data Using Real-Time Quantitative Pcr and the 2−Δδct Method. *Methods* **2001,** *25*, 402-408.

GRAPHICAL TABLE OF CONTENTS:

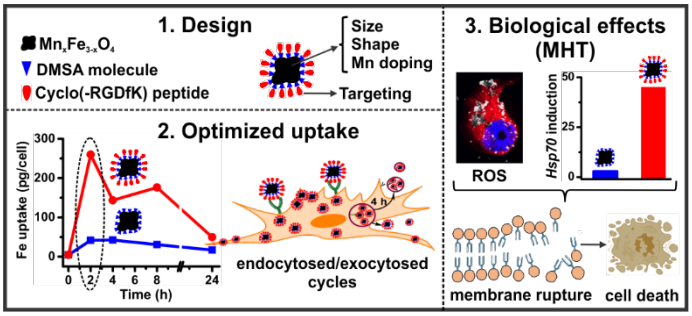
1. Design
$Mn_xFe_{3-x}O_4$
DMSA molecule
Cyclo(-RGDfK) peptide
Size
Shape
Mn doping
Targeting
2. Optimized uptake
Fe uptake (pg/cell)
300
200
100
0
0
2
4
6
8
24
Time (h)
4 h
endocytosed/exocytosed cycles
3. Biological effects (MHT)
ROS
Hsp70 induction
50
25
0
membrane rupture
cell death